Master's Thesis
석사 학위논문

Ab-Initio Computational Studies of the Catalysis Mechanisms on Graphene-Based Materials in Fuel Cell Applications

In Hye Kwon (**권 인 혜 權 仁 惠**)

Department of Energy Systems Engineering

에너지시스템공학전공

DGIST

2013

Master's Thesis
석사 학위논문

Ab-Initio Computational Studies of the Catalysis Mechanisms on Graphene-Based Materials in Fuel Cell Applications

In Hye Kwon (**권 인 혜 權 仁 惠**)

Department of Energy Systems Engineering

에너지시스템공학전공

DGIST

2013

Ab-Initio Computational Studies of the Catalysis Mechanisms on Graphene-Based Materials in Fuel Cell Applications

Advisor: Professor Byungchan Han

Co-advisor: Doctor Hoyoung Kim

By

In Hye Kwon
Department of Energy Systems Engineering
DGIST

A thesis submitted to the faculty of DGIST in partial fulfillment of the requirements for the degree of Master of Science in the Department of Energy Systems Engineering. The study was conducted in accordance with Code of Research Ethics[1]

12. 05. 2012

Approved by

Professor Byungchan Han (Signature)
(Advisor)

Doctor Hoyoung Kim (Signature)
(Co-Advisor)

[1] Declaration of Ethical Conduct in Research: I, as a graduate student of DGIST, hereby declare that I have not committed any acts that may damage the credibility of my research. These include, but are not limited to: falsification, thesis written by someone else, distortion of research findings or plagiarism. I affirm that my thesis contains honest conclusions based on my own careful research under the guidance of my thesis advisor.

Ab-Initio Computational Studies of the Catalysis Mechanisms on Graphene-Based Materials in Fuel Cell Applications

In Hye Kwon

Accepted in partial fulfillment of the requirements
for the degree of Master of Science.

12. 05. 2012

Head of Committee _____ (Signature)
Prof. Byungchan Han

Committee Member _____ (Signature)
Dr. Hoyoung Kim

Committee Member _____ (Signature)
Prof. Hasuck Kim

MS/ES

201124001

권인혜. In Hye Kwon. Ab-Initio Computational Studies of the Catalysis Mechanisms on Graphene-Based Materials in Fuel Cell Applications. . Department of Energy Systems Engineering. 2013. 46P. Advisor Prof. Byungchan Han, Co-Advisor Dr. Hoyoung Kim

Abstract

Low temperature fuel cells with noble metal-based catalysts are one of the promising green technologies. However, they have obstacles to wide commercialization largely caused by catalysts with high materials costs, poor electrochemical durability, and low efficient activity. As such, it is highly demanded to develop inexpensive but efficient and stable metal-free catalysts of fuel cells. Recently, it was reported that the electrochemical activity of nitrogen-doped graphene for oxygen reduction reaction (ORR) could be comparable to Pt/C in alkaline fuel cells.

In this thesis, catalytic mechanisms of graphene-based materials for Polymer Electrolyte Membrane Fuel Cells (PEMFCs) were studied using first-principles density functional theory (DFT) computations. Thesis work includes the atomic-level structural studies of graphene-based materials, charge distribution analysis by doping, interfacial water layer structures, adsorption energies of various chemical species. These quantum mechanical grade of information is used to construct thermodynamic free energy diagrams and thus, to identify the most viable ORR mechanisms.

This thesis confirms that doping with heteroatom in graphene causes charge redistribution, and creates charged sites. Positively charged sites with lower electronegativity between carbon and dopants acted as O_2 adsorption sites by reducing overpotential needed in the O_2 adsorption. Furthermore, two-electron reaction involving hydrogen peroxide was not preferred on N, B, and P-doped graphene but on pristine graphene.

Through this thesis, we found doping with heteroatoms can considerably affect the electronic structures of graphene and alter its ORR mechanisms leading to improving ORR activity.

Keywords: first-principles, density functional theory, fuel cell, oxygen reduction reaction, graphene

Contents

List of Figures

List of Tables

Chapter 1

Introduction

1.1 Overview

Science and technologies harvesting energy from fossil fuels have been a major role in establishing our modern civilization. Nevertheless, serious humankind's environment degradation and securities of the finite resources of fossil fuels have driven to develop clean renewable energy sources. For example, in March, 2007, the European Union declared to replace 20% of all energy consumption with renewable energy in year of 2020. Lewis and Nocera[1] have stated that the supply of clean, safe, and sustainable energy is certainly the most important scientific challenge which human beings face in the 21st century.

Fuel cells (FCs) have received intensive attention because they have high energy conversion efficiency without emission of any pollutants causing damage to environment. Fuel cells are devices that convert the chemical energy of fuels directly to electric energy. It was first made by William Robert Grove in 1839 by exposing hydrogen and oxygen gas to a sulfuric acid bath in the presence of porous platinum (Pt) electrodes. The reactions of FCs are demonstrated from Eqs.(1.1) to (1.3) where SHE represents the standard hydrogen electrode, and the schematic of a fuel cell is shown in Fig.1.1.

$$\text{Anode reaction: } 2H_2 \rightarrow 4H^+ + 4e^- \ (E_{anode} = 0.00V \ vs \ SHE) \quad (1.1)$$

$$\text{Cathode reaction: } O_2 + 4H^+ + 4e^- \rightarrow 2H_2O \ (E_{cathode} = 1.23V \ vs \ SHE) \quad (1.2)$$

$$\text{Overall reaction: } 2H_2 + O_2 \rightarrow 2H_2O \ (E_{cell} = 1.23V \ vs \ SHE) \quad (1.3)$$

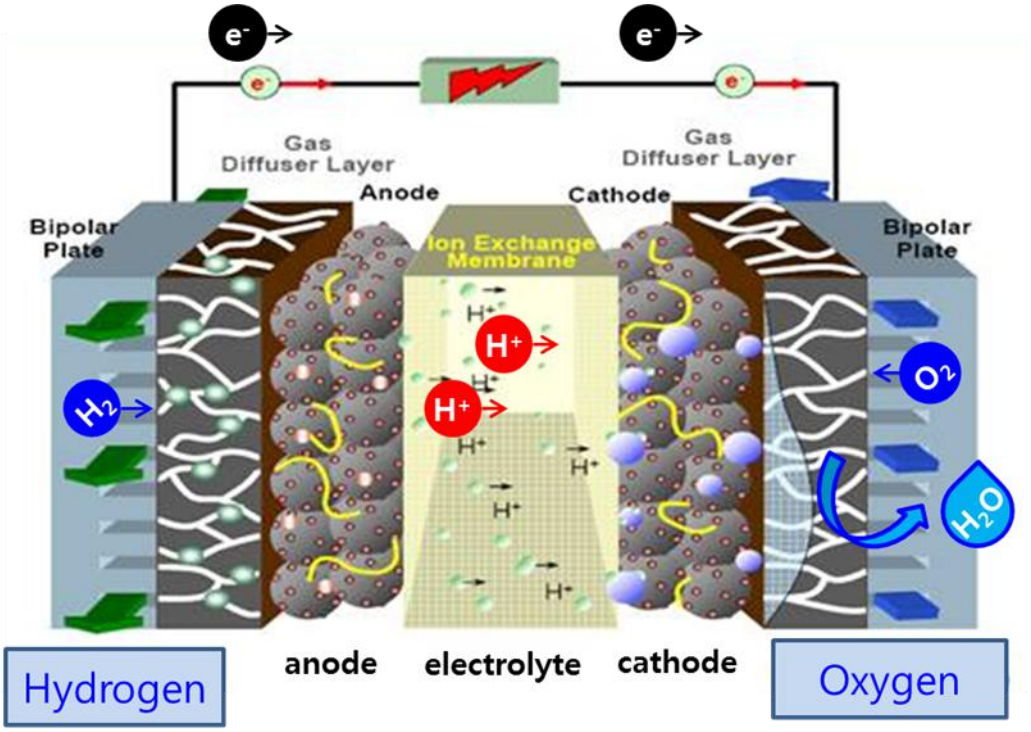

Fig.1.1 Schematic of Polymer Electrolyte Membrane Fuel Cells (PEMFCs) [2]

As oxygen reduction reaction (ORR) is kinetically very slow in low temperature fuel cells such as PEMFCs, catalysts must be used to facilitate this reaction. Conventionally platinum and its alloys have been utilized as the catalysts.[3-5] It is indeed, shown that novel Pt-M alloy nanoparticles (M= Co, Ni, Fe, Cu, Cr, etc.) could be highly active catalysts.[6-8] Nørskov et al. explained that the electronic structure of Pt (d-band center) is modified by the alloying elements leading to weaker oxygen binding strength.[9] The electrochemical stability of these nanoscale alloys, however, was reported to be much weaker than that of bulk Pt.[10-12] For example, the 3d metals dissolve into acidic media[10] or the particles grow to larger size either by agglomeration or electrochemical dissolution followed by re-precipitation into bigger particles[11]. Besides, the high material cost of noble metal catalysts is another challenge. In Fig. 1.2, the largest portion of the fuel cell stack price is occupied by the catalyst ink and application. The pie chart indicates that the catalyst is a main factor of the high price of the fuel cell stack.

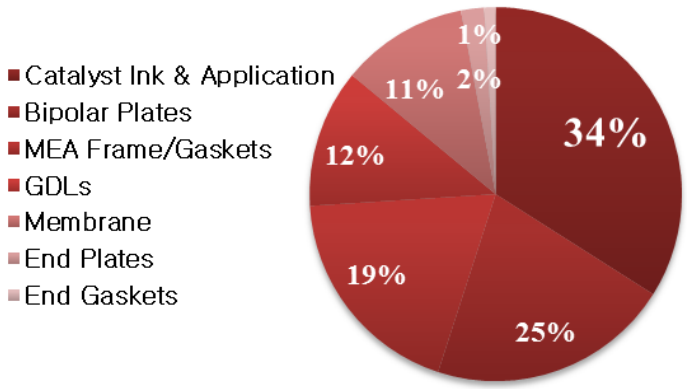

Fig.1.2. Fuel cell stack cost[13]

For the above reasons, fuel cells have not been widely commercialized yet in spite of the high interests and focused researches. As such, there have been investigations to develop non-precious metal catalysts with high efficiency and long-term stability for ORR. For example, carbon materials such as carbon nanotube (CNT), carbon nanoribbon, and graphene have received a lot of attention due to their superior electronic conductivity and physical stability.[14] Particularly, fascinating properties of graphene such as high surface area (2,630 m^2/g),[15] fast charge carrier mobility (~200,000 $cm^2 V^{-1}s^{-1}$),[16] and strong Young's modulus (~1 TPa)[17] have made graphene as a promising catalyst material. Furthermore, it has been recently reported that the electrochemical activity of nitrogen (N)-doped graphene for ORR is comparable to Pt/C in alkaline fuel cells.[18,19]

In this thesis, we focus on catalytic mechanisms of graphene-based materials for ORR in fuel cells, and expect that this study contributes to developing new metal-free catalysts via understanding of their fundamental electrocatalytic mechanisms in atomistic scale.

1.2 Literature Review

Understanding of the electrochemical reaction at atomic scale is an important step toward investigation on fundamental mechanisms of ORR, leading to development of new metal-free catalysts. Therefore, a great number of computational works have been reported which have studied oxygen reduction reaction on non- metallic carbon nanomaterials.[19-27] Anderson et al. investigated ORR on N-doped carbon using experiment and B3LYP hybrid Density Functional Theory (DFT) method.[25] They showed oxygen is reduced to hydro peroxide in the acidic condition on the graphite materials. Although the reaction proceeds through two-electron reduction in their study, their work stimulated the research of non-platinum group metal (PGM) catalysts. Referring to this study, Okamoto demonstrated that the polarization of carbon (C)-nitrogen (N) bonds as well as high spin density at carbon atoms adjacent to nitrogen plays an important role in ORR on N-doped graphene.[24] He considered graphene structures with 3.125%, 6.25%, 9.375%, and 12.5% of nitrogen concentrations, and demonstrated that the repulsion between an oxygen molecule and N-doped graphene decreased as the amount of nitrogen in the model increased. He said this is caused by C-N bonds polarization, and we will examine this using Bader charge analysis in this study. [28-30]

Liang et al. [27] on the other hand, presented the overall energy profile of oxygen reduction reaction including the energy barriers to acquire the basic chemistry of ORR on N-doped graphene. Contrary to previous works, they simulated in an alkaline condition, and they derived the free energy of OH^- as $G(OH^-) = G(H_2O) - G(H^+)$. Also, they compared association and dissociation mechanisms for ORR, and concluded the former is preferred to the latter thermodynamically.

Lipeng et al. [31] demonstrated that ORR on N-doped graphene is a four-electron mechanism, which is consistent with the previous experimental results[18]. They showed the relative energy states of intermediates of ORR for two reaction pathways as shown in Fig.1.3.

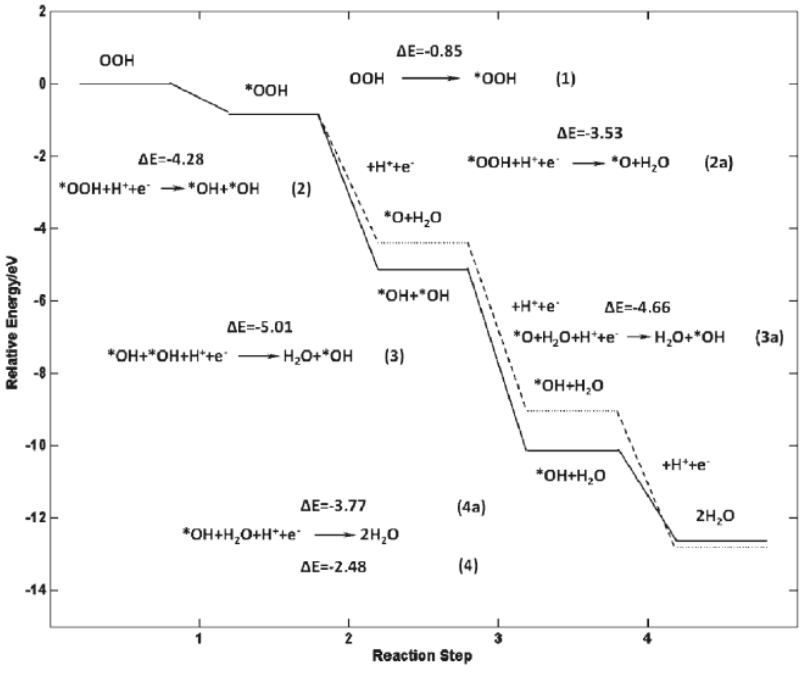

Fig.1.3 Relative energies of two different reaction pathways of the ORR on N-doped graphene. For the first step, the reference energy state is the total energy of optimized N-doped graphene and OOH molecules, and for the other reaction steps, the reference energy states are the total energy of the product of previous reaction and $H^+ + e^-$.[31]

Furthermore, they elucidated that the catalytic active sites on the N-doped graphene depend on the atomic charge and spin density distribution as shown in Fig.1.4.

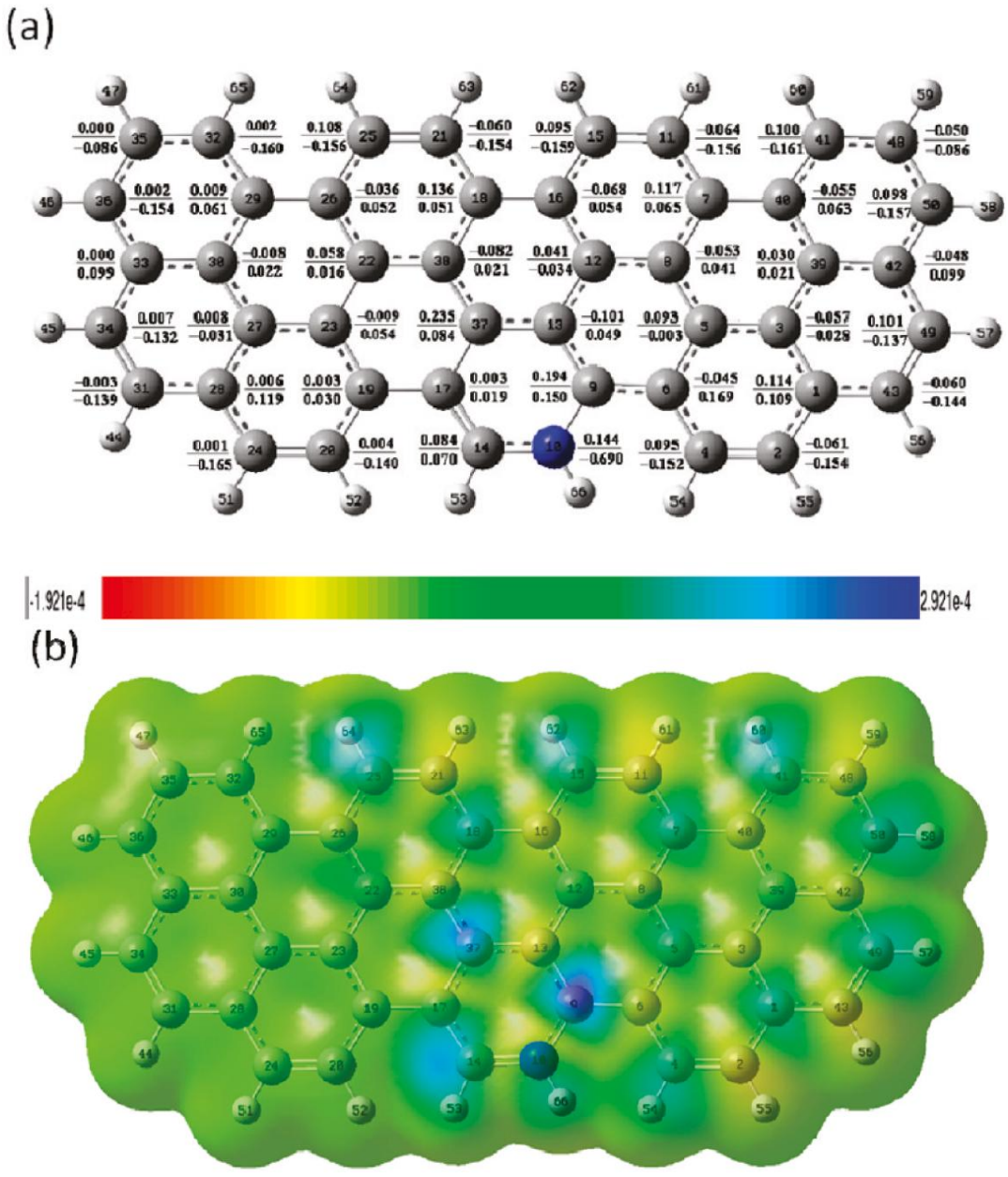

Fig.1.4 (a) Charge distribution and (b) spin density distribution on N-doped graphene with pyridine structure. The number on the circle is the number of atom. The denominators of the fractions on the side of atoms in (a) are the charge values while the numerators are the spin densities. In (b), spin density distributes on the isosurface of electron density; the most negative value is red while the most positive value is blue.[31]

In Fig. 1.4, they found the second-nearest neighbor carbon atom has the largest atomic charge while the nearest has the second largest value, and a carbon at the opposite position of the nitrogen in the same hexagon ring has the biggest spin density while the nearest has the second biggest value. They calculated the adsorption energy of an OOH molecule on the carbon atoms to find the active site, and concluded the nearest carbon to nitrogen atom is the most active with high spin density and atomic charge density.

The above pioneering works shed a light on the preliminary understandings of ORR mechanisms catalyzed by N-doped graphene. However, structural studies of N-doped graphene and interfacial water structures remain unclear. Detailed studies to obtain more accurate understanding about ORR in the atomistic scale, which is the key to develop new metal-free catalysts, are discussed in this thesis work.

1.3 Thesis Outline

This thesis focuses on fundamental catalytic mechanisms of graphene-based materials which can be potential alternatives to noble metal catalysts in Polymer Electrolyte Membrane Fuel Cells (PEMFCs). The goal of this thesis is to understand why and how doping with heteroatoms can change the electrocatalytic activity of graphene. Despite extensive experimental[18,20,32] and theoretical studies[24,27], the atomic level agreement on the detailed catalytic mechanisms on doped-graphene is still missing. In this thesis, we utilized ab-initio DFT calculations to achieve the goal. Specifically, thermodynamically stable interfacial water structures are identified at electrode-electrolyte near the surface of graphene-based materials. Starting from this, ORR mechanisms were investigated aiming to determine the electrocatalytic activity of graphene-based materials.

Chapter 1 described challenges of Pt catalysts in fuel cells and introduced thesis objectives in overview. The motivation of this thesis was created by a careful review of previous literatures on the ORR mechanisms on carbon-based materials summarized in Chapter 1. Chapter 2 introduces the ab-

initio DFT computation method and explains details this thesis utilized. The results of thesis work are demonstrated in Chapter 3 which consists of five subsections;

(1) ab-initio thermodynamics identifying stable structures of nitrogen-doped graphene as a function of the nitrogen doping level,

(2) charge density analysis after doping of hetero atoms such as boron (B), nitrogen (N), and phosphorus (P),

(3) interfacial water structures between the electrolyte and graphene,

(4) relaxed structures and energies of an adsorbed O_2 molecule and OH on graphene-based materials, and

(5) ORR mechanisms of different graphene-based materials.

The conclusions in Chapter 4 will summarize this thesis work.

Chapter 2

Methodology

2.1 Introduction to the Ab-Initio Computations

To investigate material properties and design new materials, experimental and computational approaches are available. In this thesis, the electrocatalytic reactions of graphene-based materials in fuel cells were studied using the ab-initio Density Functional Theory (DFT) computations. When systems with molecular or atomic levels are studied, computational approaches have several advantages over experiments. They can control the experimental parameters exactly and avoid perturbations between constituent atoms and experimental variables. Although the accuracy is dependent on the scientific laws accompanied by modeling, computational methods are very powerful and effective to predict material properties (electric, optical, magnetic, and mechanical properties) in the atomistic scale.

First-principles computations use only established fundamental physical laws without any empirical parameters or assumptions, and find material properties by solving the Schrödinger equation directly based on quantum mechanics.[33] By solving this equation, system energies, charge densities, and band structures can be obtained, which can provide the quantitative information related to material properties. They can be highly logical, but have a limitation of the number of atoms which can constitute the model systems due to finite computational capability. However, the rapid development of computer science, hardware and software industries has brought an expansion of this first-principles computational approach to a variety of scientific fields. More details on the first-principles DFT can be found in Ref.34 [34]

2.2 Computational Details

We utilized DFT[35,36] calculations implemented in the Vienna Ab-initio Simulation Package (VASP) program.[37] The exchange-correlation energy of electrons is described by the Perdew, Burke and Ernzerhof (PBE) functional[38] under generalized gradient approximation (GGA)[37]. Interaction potentials of core electrons were replaced by the projector augmented wave (PAW) pseudo-potentials,[39,40] and we expanded wave functions of valence electrons using a plane wave basis set with a cutoff energy of 400 eV.

We imposed a periodic boundary condition with a vacuum region of 13.6 Å for the graphene sheets which is large enough to avoid interplanar interactions. The calculated C-C bond length of a graphene sheet was 1.420 Å, which is close to the measured value of 1.418 Å[24]. All adsorbates and graphene sheets were fully relaxed to optimize the structures.

To sample the Brillouin zone, a Gamma point mesh of 15 x 15 x 1 was used for the graphene (1x1) unitcells, and smaller meshes for larger supercells. We observed that this k-points sampling allowed the total energy of the graphene model systems to converge within 20 meV.

2.3 Bader Charge Analysis

To investigate the change of electronic charge density in graphene by doping, we used Bader charge analysis.[30] Richard Bader, from McMaster University, developed an intuitive way of dividing molecules into atoms called the Quantum Theory of Atoms In Molecules (QTAIM). According to his definition, an atom is based purely on the electronic charge density, and the charge density reaches a minimum between atoms in molecular systems as in Fig.2.1.

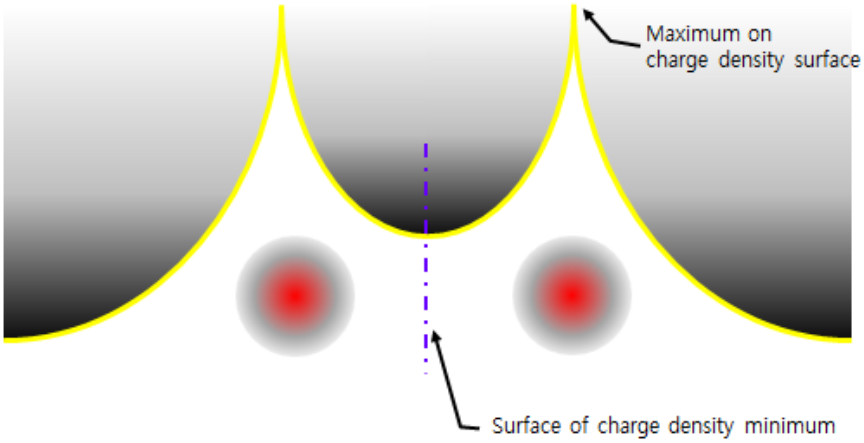

Fig.2.1 Schematic of an atom based on Bader's definition

Bader's theory of atoms in molecules is often useful for charge analysis. For example, the charge distribution can be utilized to determine multipolar moments of interacting atoms or molecules. Also, this can provide a definition for chemical bonding which gives numerical values for bond strength.

We calculated the charge density of graphene-based materials using the Bader program which is computational method for partitioning a charge density grid into Bader volumes as in Fig.2.2.

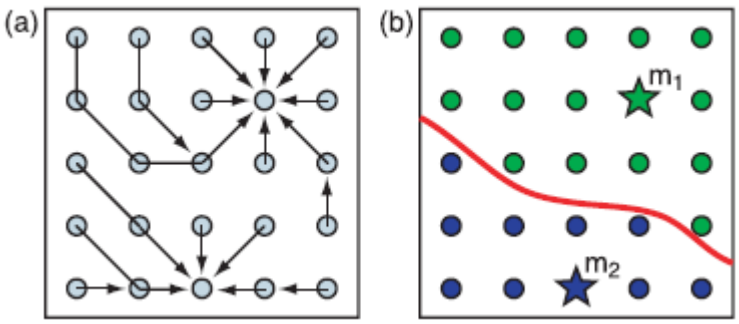

Fig.2.2 An illustration of the steepest ascent paths (a) on a charge density grid to find the Bader volumes using the on-grid analysis method. These ascent trajectories are constrained to the grid points, moving at each step to the neighboring grid point towards which the charge density gradient is maximized. Each trajectory either terminates at a new charge density maximum, m_i, or at a grid point which has already been assigned. After all grid points are assigned (b), the set of points which terminate at each maximum (green to m1 and blue to m2) constitutes the Bader volumes. The Bader surfaces (red curved line) separate the volumes.[41]

Chapter 3

Results and Discussion

In this chapter, the computational results aiming to obtain fundamental understanding of ORR mechanisms on graphene-based materials are explained with numerical energy values and visualized structures.

3.1 Stable Structures of Nitrogen-Doped Graphene

To find the thermodynamically stable N-doped graphene structure, we calculated the energies of 98 structures with seven kinds of supercells and a nitrogen concentration ranging from zero to 100%. We assumed a nitrogen atom replaces a carbon atom in the graphene framework by substitution. Using these energies we constructed the energy convex hull. $\Delta E_{doping}(x)$ of each structure was calculated by the equation

$$\Delta E_{doping}(x) = E_{DFT}(x) - \left\{ \left[E_{DFT}(\theta_N = 1) - E_{DFT}(\theta_N = 0) \right] x + E_{DFT}(\theta_N = 0) \right\} \qquad (3.1)$$

where x is the concentration of nitrogen (N) in the graphene framework, and $E_{DFT}(x)$ is the energy of each structure calculated by DFT when N concentration is *x*. $E_{DFT}(\theta_N = 0)$ and $E_{DFT}(\theta_N = 1)$ are DFT calculated energies when the concentrations of N in the graphene are zero and one, respectively.

$\Delta E_{doping}(x)$ can be regarded as the additional stability of each structure, which indicates how much this structure is energetically stable relative to that of a homogeneous local environment at the same concentration x.[42] In Fig.3.1, the energy convex hull constructed from $\Delta E_{doping}(x)$ of the

calculated structures shows their relative chemical stabilities.

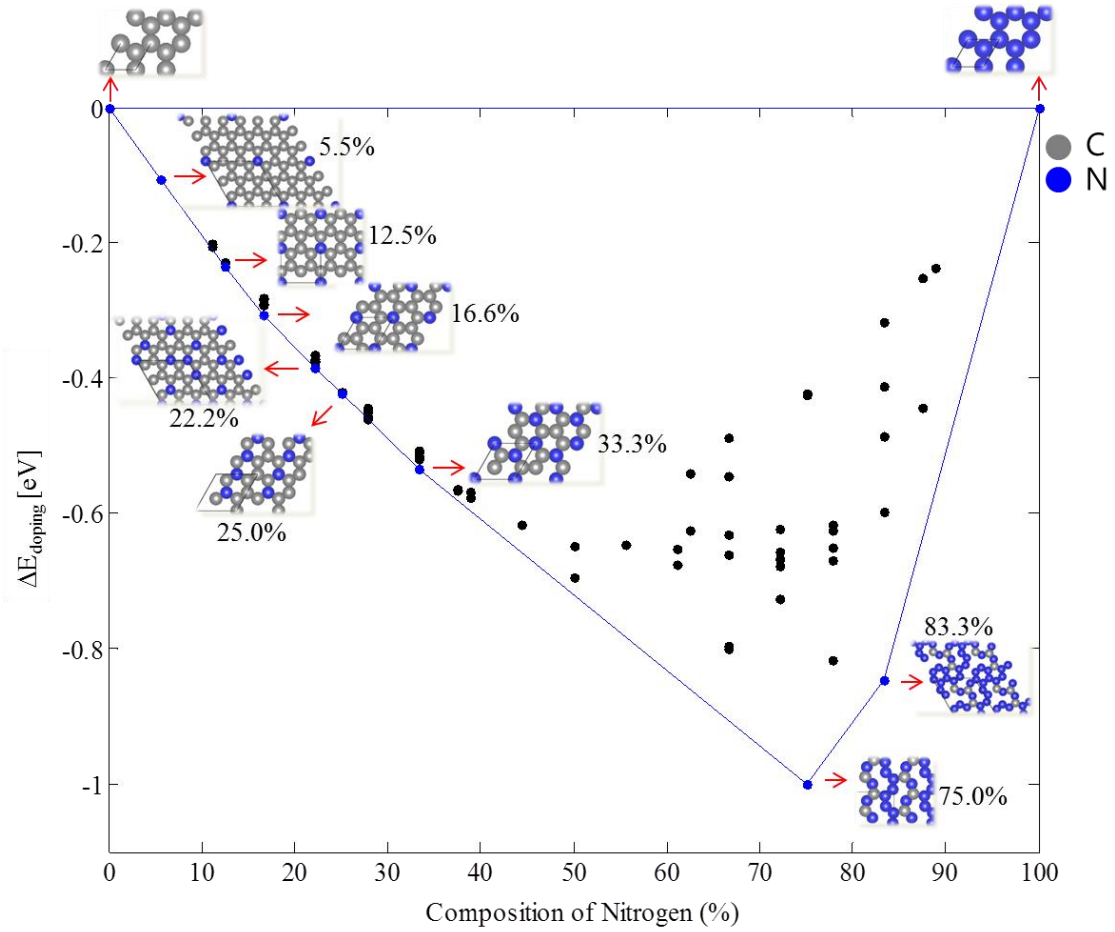

Fig.3.1 Ab-initio calculated energy convex hull diagram of the nitrogen doped graphene as a function of nitrogen concentration. Black and blue dots denote the ab-initio calculated 98 structures of different nitrogen atomic concentrations and configurations. Blue dots indicate the ground state structures. Their detailed morphologies were inserted with arrows at each concentration.

At over 50% of nitrogen atomic concentration, two structures on the energy convex hull have the broken hexagonal framework. This implies that it is hard to maintain the graphene framework when more and more nitrogen atoms are introduced into the graphene.

We selected the structure with 5.5 at% of nitrogen out of ten ground state structures for our calculation model as shown in Fig.3.2, considering the previous experimental synthesis results have shown around 4~5 at% of nitrogen in the graphene.[18,43,44] This structure is a (3×3) cell, and one

carbon atom is replaced by a nitrogen atom. In this structure, the distances between the carbon and the nitrogen atoms in the model only changed from 1.42 to 1.41 Å after relaxation because of the similar atomic radiuses of carbon (0.77 Å) and nitrogen (0.74 Å). From the next section, these structures are used as model systems for calculations.

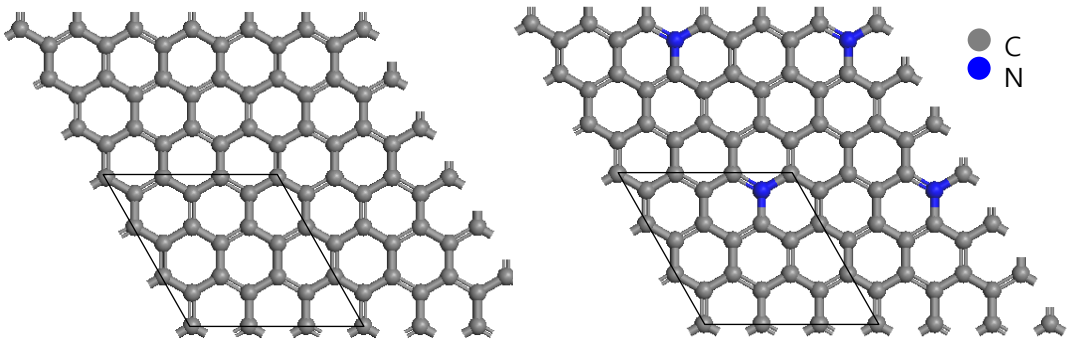

(a) Pristine graphene (b) N-doped graphene (5.5 %)

Fig.3.2 Schematic top views of the model systems used for the (a) pristine graphene and (b) N-doped graphene. Grey and blue spheres indicate carbon and nitrogen atoms respectively.

3.2 Charge Density Analysis

Previous studies have reported that when heteroatoms are incorporated in carbon materials, the electronic structure as well as the chemical properties changes.[45-49] Furthermore, the electronic structure changes were attributed to enhanced catalytic activity of N-doped carbon materials.[24,31,32,50] This means ORR activity and mechanisms are strongly influenced by the electronic properties. To investigate the details related to the change in electronic properties caused by doping, we calculated charge density changes and atomic partial charges using Bader charge analysis as introduced in Chapter 2.3. For comparison, we calculated the charge density changes of nitrogen (N), boron (B) and phosphorus (P)-doped graphene in the same condition. Fig 3.3 shows the charge density changes after doping.

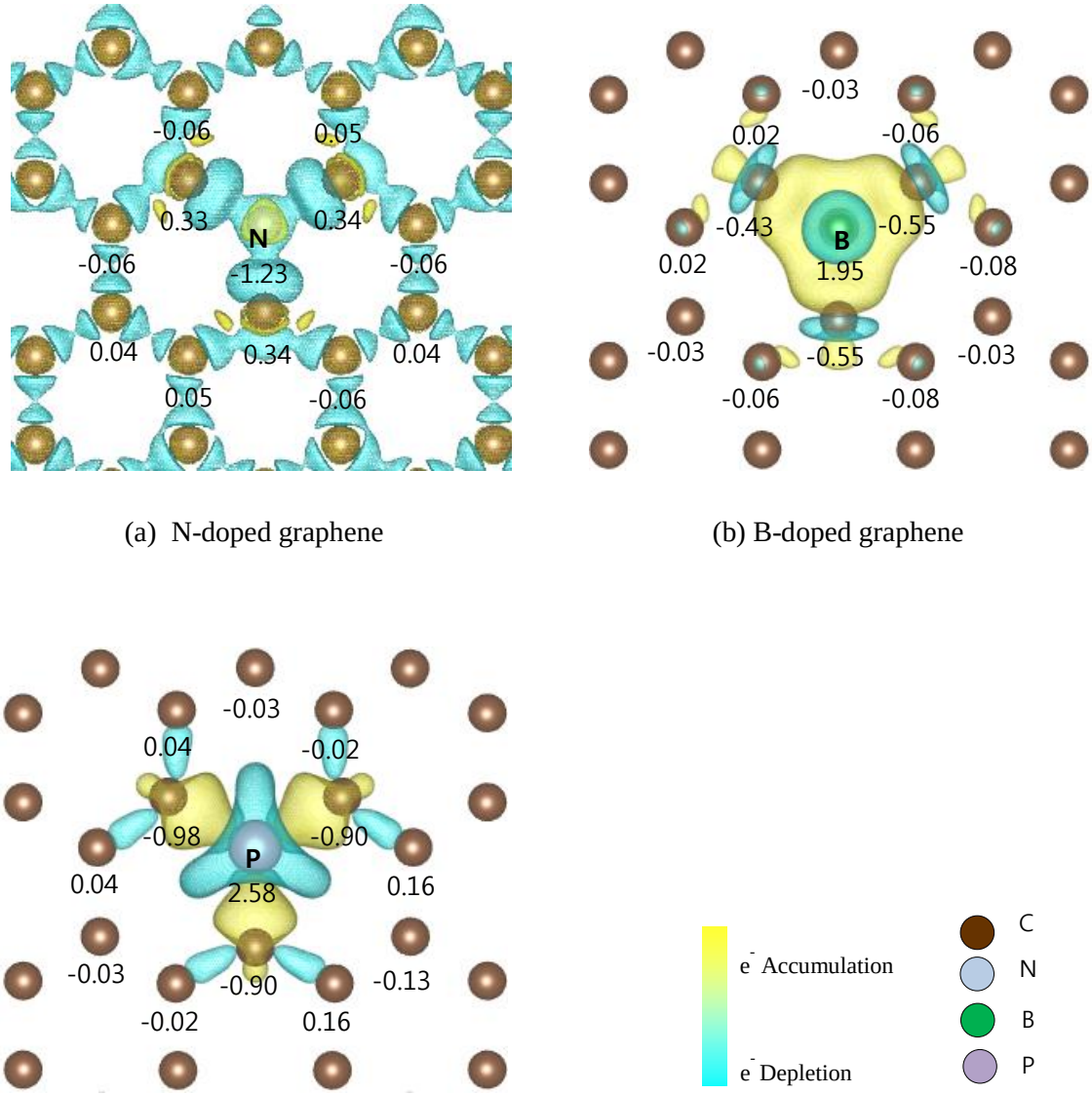

(a) N-doped graphene

(b) B-doped graphene

(c) P-doped graphene

Fig.3.3 Charge density changes of (a) N-doped, (b) B-doped, and (c) P-doped graphene respectively. Charge density changes were calculated as follows, $\Delta\rho = \rho_{XG} - \rho_G + \rho_C - \rho_X$, where ρ_{XG}, ρ_G, ρ_C, and ρ_X represent Bader charges of X-doped graphene, graphene, a carbon atom, and a dopant X atom, respectively.

When a nitrogen atom is doped to a graphene, the nitrogen showed a negative charge of -1.23e while boron and phosphorus atoms which were doped in the same supercells showed positive charges of 1.95e and 2.58e, respectively. Moreover, three neighbor carbon atoms bonded to the nitrogen

showed positive charges of 0.33 ~ 0.34*e*, while three adjacent to the boron and phosphorus showed -0.43 ~ -0.55*e* and -0.90 ~ -0.98*e*, respectively. This can be explained by the difference in electronegativity between carbon and heteroatoms. Nitrogen has a higher electronegativity (3.0) than carbon (2.5), so it can draw electrons from neighboring carbons. In contrast, boron (2.0) and phosphorus (2.1) have lower electronegativity than carbon; therefore, their electrons are attracted to the adjacent carbon atoms.[51] Moreover, the magnitude of doping-induced partial charges gets smaller as the distance gets further from the dopants, as in Fig. 3.4. It is clear that the nearest three carbon atoms are most strongly affected by the dopant and show the largest amount of partial charges.

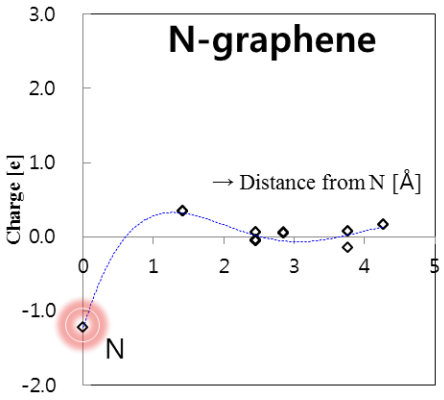

(a) N-doped graphene

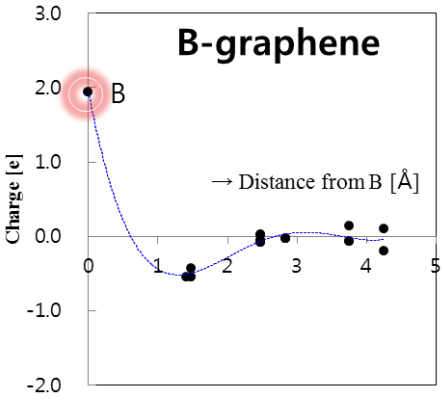

(b) B-doped graphene

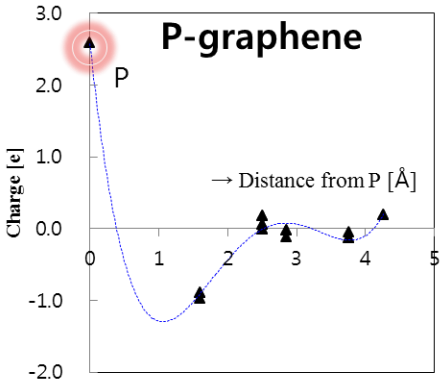

(c) P-doped graphene

Fig.3.4 Atomic charges of (a) N, (b) B, and (c) P-doped graphene, respectively, as a function of the distance from the dopant atom. Blue dotted lines are fitted lines.

To investigate the effect of the cell size on the Bader charge, we calculated for different size supercells: $(1\times1),(\sqrt{3}\times\sqrt{3}),(2\times2),(3\times3),(4\times4),(5\times5)$, and (6×6). As in Fig. 3.5, the charge of a nitrogen atom converges to -1.5e. Furthermore, the ratio of $|\rho_N|$ to $|\rho_C|$ converges to three, where $|\rho_N|$ is the absolute charge of the nitrogen, and $|\rho_C|$ is the average absolute charge of the three carbon atoms adjacent to the nitrogen atom. This indicates that the negative charge of the nitrogen is almost compensated for by the sum of the positive charges of the three neighbor carbon atoms.

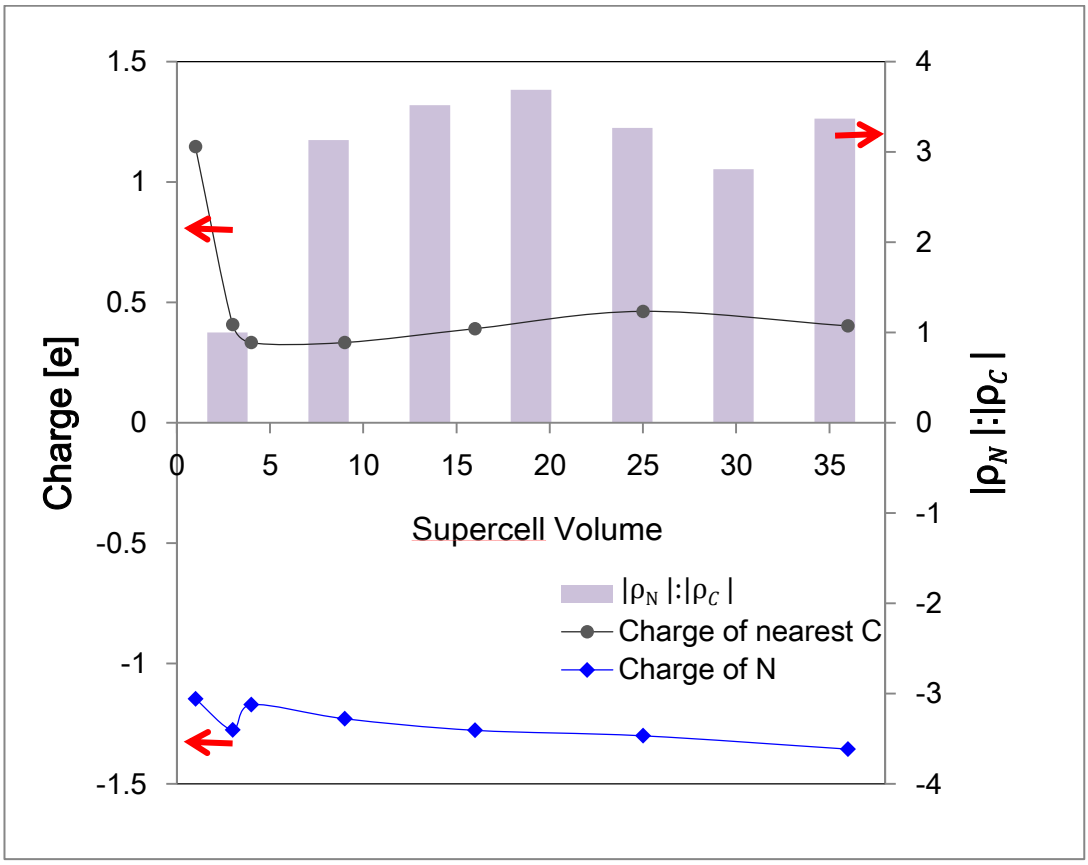

Fig.3.5 Charge density change of N-doped graphene with different supercell sizes. $|\rho_N|$ is the absolute charge of a nitrogen atom, and $|\rho_C|$ is the average absolute charge of the three carbon atoms adjacent to the nitrogen atom.

In Fig.3.6, Bader charges of carbon, boron, and nitrogen atoms were compared as a function of

electronegativity. This figure shows that an atom with higher electronegativity possesses the more negative charge, as expected.

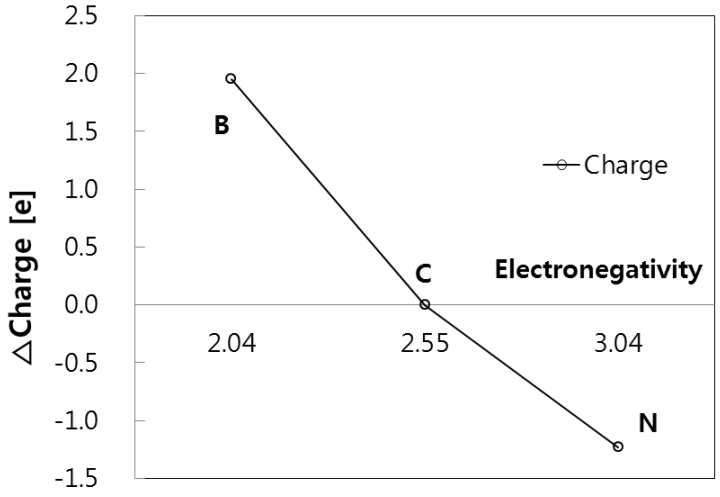

Fig.3.6 Bader charges of atoms doped in graphene sheets as a function of electronegativity. B, C, and N represent boron, carbon, and nitrogen, respectively. C indicates carbon in pristine graphene.

3.3 Interfacial Water Structures

Prior to studying the oxygen reduction reaction mechanisms, it is necessary to investigate the interfacial water (H_2O) structures between water and the catalyst surface because ORR not only proceeds in the water environment but also involves water molecules.

First, we investigated the effect of electric field on the H_2O adsorption because it has been reported that an electric field affects the geometry and the adsorption energies of the H_2O molecules.[52] We applied an external electric field in the perpendicular direction to the graphene sheet and calculated the adsorption energy of a H_2O molecule on the (3×3) supercell with electric fields from -0.3V/Å to 0.3 V/Å as in Fig.3.7. Because a H_2O molecule has a dipole moment, where hydrogen (H) is δ^+ and oxygen (O) is δ^-, the molecular direction varies according to the electric fields. The electric field is determined according to the difference in potentials of electrodes and the thickness of an electric double layer. Details about the electric field effect can be found in the previous study.[52] With

an electric field of -0.3 V/Å, the H_2O molecule is adsorbed on the N-doped graphene with a H atom upward. In contrast, with an electric field of +0.3 V/Å, the H_2O molecule was adsorbed with one H atom downward and one parallel.

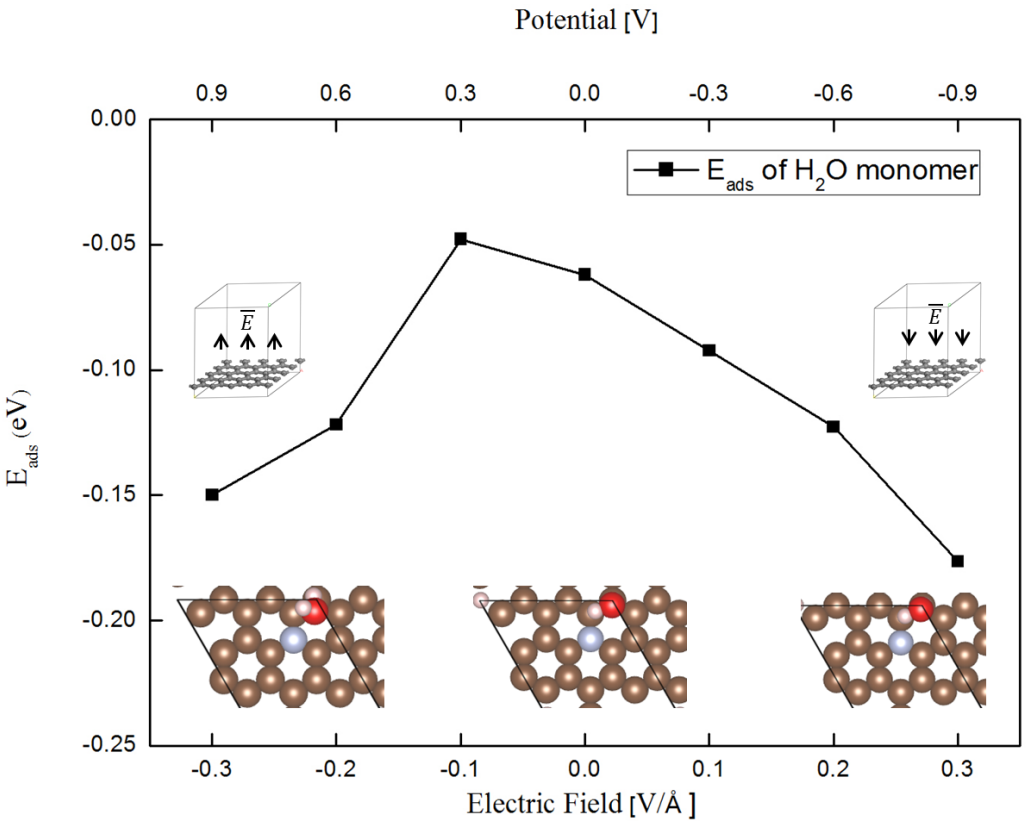

Fig.3.7 Ab-initio calculated adsorption energies of a H_2O monomer as a function of electric field. The potentials correspond to the electric fields assuming an electric double layer thickness of about 3.0 Å.[53] Structures of H_2O/N-graphene at -0.3, 0, and 0.3 V/Å are inserted. Brown, sky-blue, red, and pink spheres indicate carbon, nitrogen, oxygen, and hydrogen atoms, respectively. Arrows in the small supercells represent electric fields.

We applied an electric field of -0.3 V/Å in all calculations in this study assuming an electric double layer thickness of 3 Å[53]. -0.3 V/Å corresponds to an electrode potential of 0.9 V relative to

the SHE. In table 3.1, ab-initio calculated adsorption energies of H_2O monomers on different graphene-based materials are compared. Adsorption energy was calculated as follows,

$$E_{ads} = E_{H_2O/G} - (E_{H_2O} + E_G) \quad (3.2)$$

where E_{ads} is adsorption energy of H_2O. $E_{H_2O/G}$, E_{H_2O}, and E_G are ab-initio calculated energies of H_2O adsorbed on graphene sheets, an isolated H_2O molecule, and graphene sheets, respectively. Positive E_{ads} means the adsorption is unstable, and negative E_{ads} means there is stronger adsorption. Adsorption energy of the H_2O molecule is positive on the pristine graphene but negative on N, B, and P-doped graphene. In particular, a H_2O molecule was adsorbed very strongly on P-doped graphene compared to other graphene-based materials studied in this work.

Distances are measured from the oxygen atom of the H_2O molecule to the nearest atom (C or dopant atoms) in the graphene sheets. Distances between H_2O and the graphene-based materials seem relatively longer than those on the Pt (100) surface, and distances from O to the graphene-based materials barely change.

Table 3.1 Ab-initio calculated adsorption energies and interatomic distances of adsorbed H_2O monomers on pristine, N, B, and P-doped graphene under the electric field of -0.3 V/Å. For comparison, the adsorption energy and the distance (O-Pt) were also shown for Pt (100) surface[42]. H_2O adsorption on the Pt (100) surface is for the atop site, which is the most stable out of atop, bridge, and hollow sites.

	E_{ads} [eV]	**Distance [Å] (O-graphene)**
Pristine graphene	0.53	3.07
N-doped graphene	-0.15	3.06
B-doped graphene	-0.10	3.07
P-doped graphene	-1.60	3.09
Pt (100) surface	-0.56	2.27

We calculated the energies of 44 different H_2O/pristine and H_2O/N-doped graphene surfaces as a function of H_2O coverage y to obtain their formation energies $\Delta E(y)$ defined as

$$\Delta E(y) = E_{DFT}(y) - \left\{ \left[E_{DFT}(\theta_{H_2O} = 1) - E_{DFT}(\theta_{H_2O} = 0) \right] y + E_{DFT}(\theta_{H_2O} = 0) \right\} \quad (3.3)$$

where y is the coverage of H_2O on the graphene surface and $E_{DFT}(y)$ is the energy of each structure calculated by DFT in the same way as in chapter 3.1. $E_{DFT}(\theta_{H_2O} = 0)$ and $E_{DFT}(\theta_{H_2O} = 1)$ are DFT calculated energies when the coverage of H_2O on the graphene is zero and one, respectively. We considered one adsorption site for one water molecule in every graphene (1×1) unitcell. Similar to chapter 3.1, an energy convex hull is constructed from all of the structures in Fig.3.8. $\Delta E(y)$ can be regarded as the additional stability of each structure, and indicates how much this structure is energetically stable relative to that of a homogeneous local environment at the same concentration y.[42]

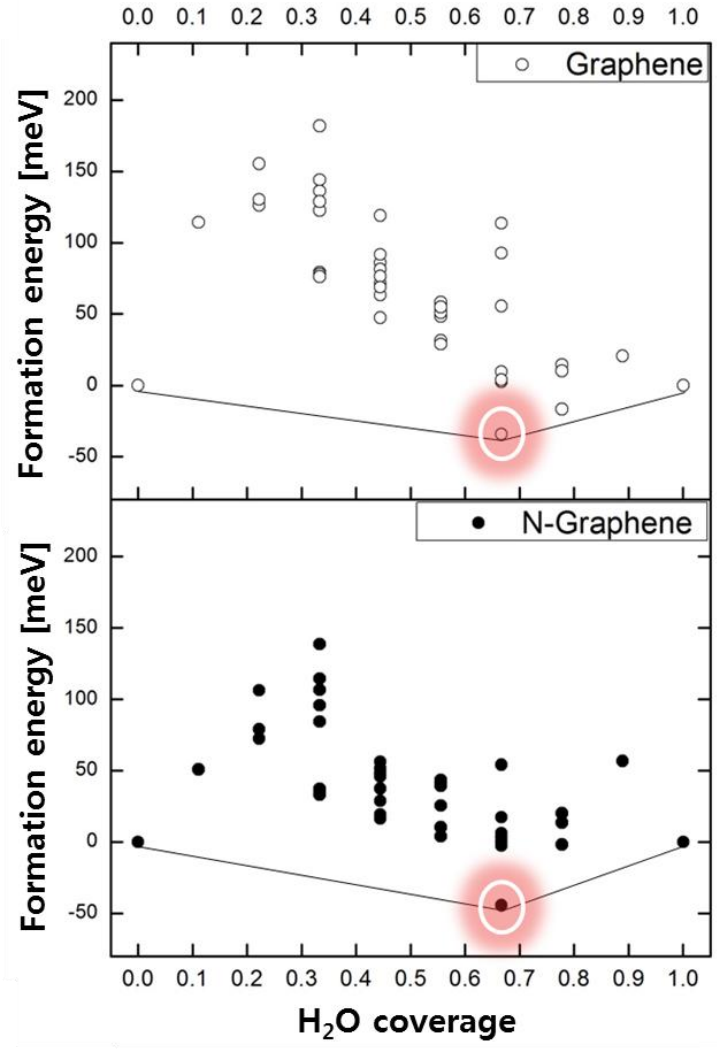

(a)

(b) (c)

Fig.3.8 Ab-initio calculated energy convex hull of H_2O on the pristine graphene (top) and N-doped graphene (bottom) as a function of H_2O coverage (a), and schematics of the ground state structures of pristine graphene (b) and N-doped graphene (c).

In Fig.3.8, it is seen that adsorption of water molecules on the pristine and N-doped graphene are not stable overall judging from the positive $\Delta E(y)$, which implies graphene is hydrophobic.[54] However, only one structure with the $2/3$ coverage of H_2O showed minus $\Delta E(y)$, implying it has additional stability. This structure shows hexagonal ring-shaped H_2O molecules with parallel and vertical H_2O molecules arranged by turns. Hexagonal ring-shaped H_2O molecules have already been reported in the case of Pt (111) surfaces in previous works[53,55] and this structure is the so-called bilayer structure. In the case of pristine graphene, the bond distances between C and O atoms are 3.07 Å for parallel and 3.83 Å for vertical H_2O molecules, respectively. In the case of N-doped graphene, they are 3.00 Å and 3.69 Å in the same order, which are a little bit closer than those on the pristine graphene. These stable interfacial H_2O structures are efficiently utilized in Chapter 3.5 which investigates ORR mechanisms.

3.4 Adsorption Energies of O_2 and OH

Efficient catalysts for ORR should possess the ability to adsorb the reactants, break the bonds, form bonds, and desorb the products.[56] If some material has too strong adsorption energy of oxygen, it can hardly desorb O and OH species, and the activity will be hindered. In contrast, material with weak adsorption energy of oxygen, the activity will be limited by the transfer of electrons and protons to adsorbed O_2.

As adsorption of reactants and desorption of products are competing processes, effective catalysts must have an optimized adsorption energy for ORR intermediates. As demonstrated in the previous work, a model of the ORR leads to a volcano-shaped dependence of the activity on the oxygen adsorption energy,[9] and this illustrates Sabatier principles very well.[57] In Fig.3.9, Pt which has the optimum oxygen adsorption energy located on at the top of the volcano plot.

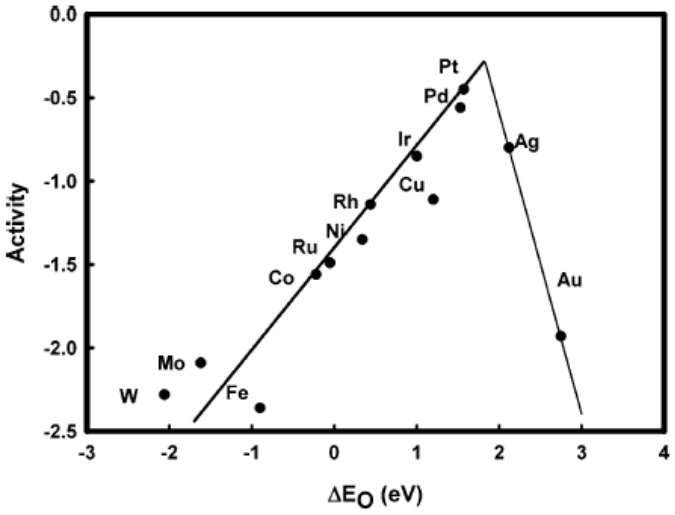

(a)

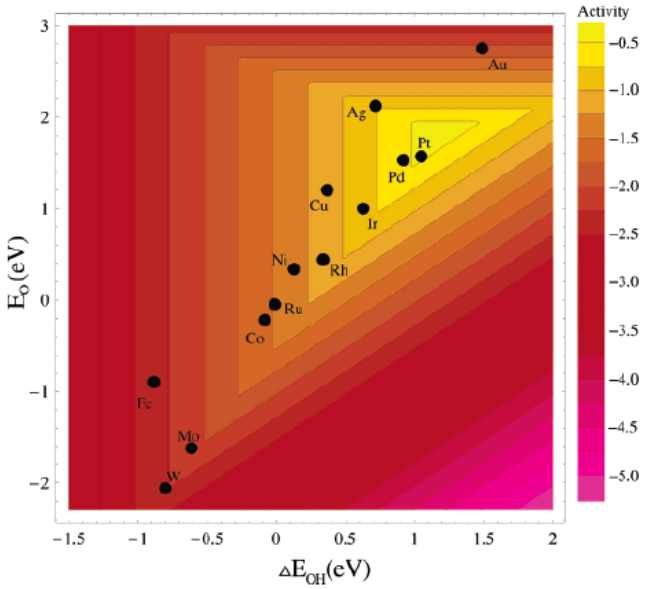

(b)

Fig.3.9 Trends in oxygen reduction activity plotted as a function of (a) O binding energy and (b) both O and OH binding energy.[58]

Here, we calculated the adsorption energies of O_2 and OH on graphene-based materials as shown in Table 3.2 as follows,

$$E_{ads} = E_{O_2,OH/G} - (E_{O_2,OH} + E_G) \tag{3.4}$$

where E_{ads} is adsorption energy of O_2 or OH. $E_{O_2,OH/G}$, $E_{O_2,OH}$, and E_G are ab-initio calculated energies of O_2 or OH adsorbed on graphene sheets, an isolated O_2 or OH, and graphene sheets, respectively.

Table 3.2 Adsorption energies and internal geometries of O_2 and OH on graphene-based materials under the external electric field of -0.3V/Å. d (O-G)[a] is the distance from the oxygen atom to the nearest carbon or dopant atom in the graphene sheets. d (O-O)[b] is the distance between two oxygen atoms, and d (O-H)[c] is the distance between oxygen and hydrogen atoms.

Adsorbates		**Pristine graphene**	**N-doped graphene**	**B-doped graphene**	**P-doped graphene**
O_2	E_{ads} [eV]	0.69	-0.85	-0.07	-2.89
	d (O-G)[a] [Å]	3.14	2.80	3.00	1.67
	d (O-O)[b] [Å]	1.29	1.31	1.29	1.59
OH	E_{ads} [eV]	-1.05	-3.01	-2.89	-6.24
	d (O-G)[a] [Å]	1.52	1.48	1.52	1.64
	d (O-H)[c] [Å]	1.00	1.00	1.00	1.00

As the adsorption energy strengthens, the distance between the oxygen and graphene sheets became shorter, as shown in Fig.3.10. Pristine graphene had a positive adsorption energy of O_2 while

heteroatom (N, B, and P)-doped graphene sheets had negative adsorption energies of O_2. P-doped graphene adsorbed O_2 the most strongly with the shortest adsorption distance, followed by N-doped graphene and B-doped graphene. Furthermore, a distance of 1.59 Å between two oxygen atoms on P-doped graphene was much longer than that on other graphene-based materials. This bond length is even longer than the isolated O_2 molecule (1.28 Å as obtained from a DFT calculation), and is comparable to O-O bond length in HOOH (1.48 Å)[24]. This implies O-O bond is dissociated by gaining electrons from graphene sheets.

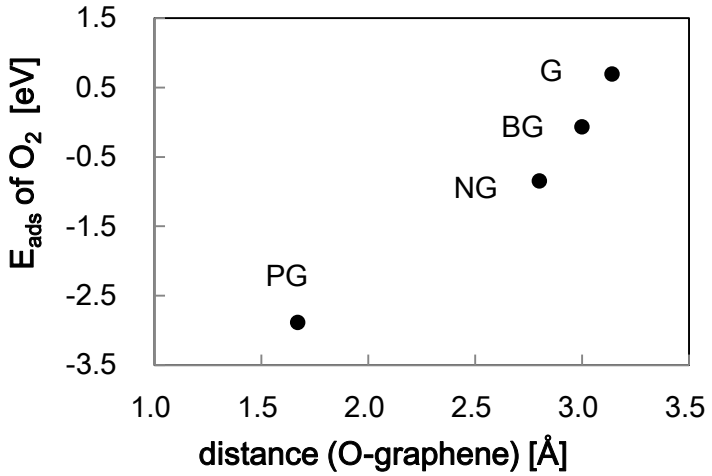

Fig.3.10 Adsorption energies of O_2 as a function of the distance between an O and the graphene sheet. G, NG, BG, and PG represent pristine, N-doped, B-doped, and P-doped graphene, respectively.

In the case of OH adsorption, all graphene-based materials showed negative adsorption energies, and the intensity of adsorption is in order of P-doped graphene, N-doped graphene, B-doped graphene, and pristine graphene. Fig.3.11 shows the relationship between adsorption energies of OH and adsorption energies of O_2. The graphene-based materials with the stronger adsorption energy of O_2 have the stronger adsorption energies of OH. This tendency is consistent with that of metals as shown in Fig.3.9.

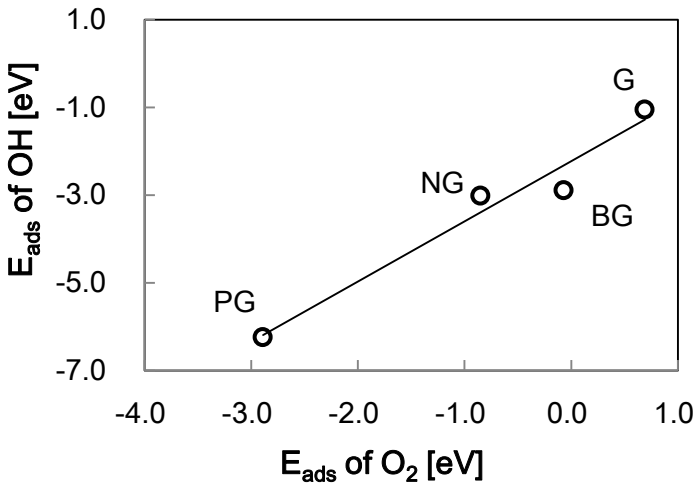

Fig.3.11 Adsorption energies of OH as a function of the adsorption energy of O_2. G, NG, BG, and PG represent pristine, N-doped, B-doped, and P-doped graphene, respectively.

Relaxed geometries and charge redistributions for O_2 adsorbed on graphene-based materials are depicted in Fig.3.12. Charge density changes were computed as follows; $\Delta\rho = \rho_{O_2/G} - (\rho_{O_2} + \rho_G)$, where $\rho_{O_2/G}$, ρ_{O_2}, and ρ_G are for Bader charges of O_2 adsorbed on graphene sheets, an O_2 molecule, and graphene sheets respectively. In the case of N-doped and P-doped graphene, charge redistributions are seen clearly, which are consistent with their stronger adsorption energies for O_2. For both cases, an increase in the electron density between the oxygen molecule and the graphene sheet is observed, while a decrease is seen at the interface of the graphene facing the oxygen molecule. Furthermore, electron density depletion is detected between oxygen atoms on P and N-doped graphene. O-O bonds seem to be cut by charge density depletion. This charge density changes also support that N and P-doped graphene have the ability to facilitate O_2 dissociation. Eduardo Cruz-Silva

et al. reported a similar result about O_2 adsorption on phosphorus-doped carbon nanotubes.[47] In their study, electron density increased between the adsorbed O_2 and the phosphorus atom, and decreased in the vicinity of the phosphorus atom.

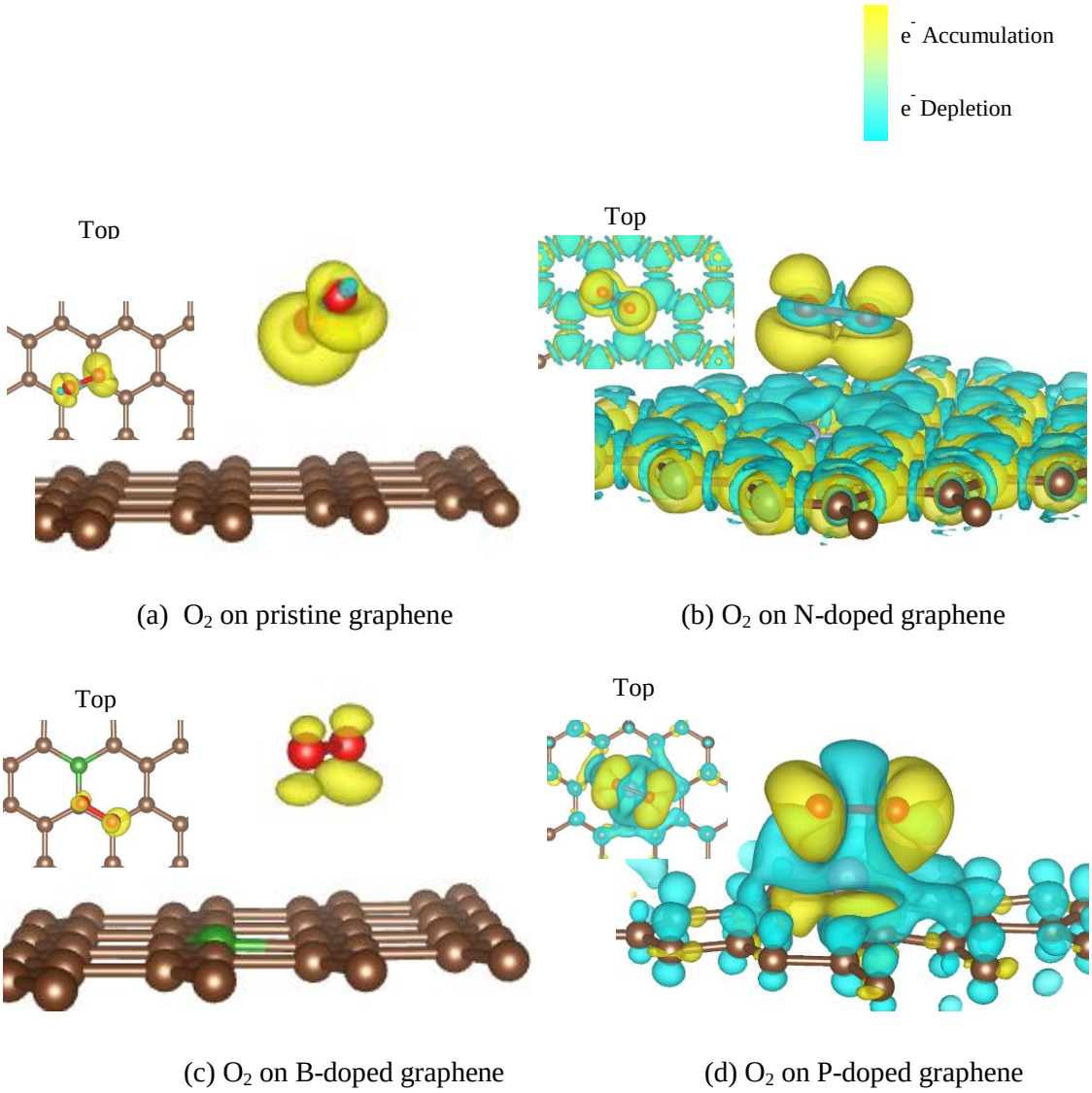

(a) O_2 on pristine graphene (b) O_2 on N-doped graphene

(c) O_2 on B-doped graphene (d) O_2 on P-doped graphene

Fig.3.12 Equilibrium geometries and charge density changes for O_2 molecules adsorbed on (a) pristine graphene, (b) N-doped graphene, (c) B-doped graphene, and (d) P-doped graphene respectively. The yellow (sky-blue) clouds represent an increase (decrease) in charge density, with isosurfaces plotted at $\pm 0.001 e$ Å^{-3}. Brown, grey, green, purple, and red spheres represent carbon, nitrogen, boron, phosphorus, and oxygen atoms respectively.

Moving from O_2 adsorption to OH adsorption, Fig.3.13 shows the relaxed geometries and charge redistributions for OH adsorbed on graphene-based materials with isosurfaces at $\pm 0.01 e \text{Å}^{-3}$. Charge density changes were computed as follows; $\Delta\rho = \rho_{OH/G} - (\rho_{OH} + \rho_G)$, where $\rho_{OH/G}$, ρ_{OH}, and ρ_G are for Bader charges of OH adsorbed on graphene sheets, an isolated OH, and graphene sheets respectively. In all cases, charge redistributions are observed clearly; i.e., increases at the vicinities of oxygen atoms and decreases at the adsorption sites on the graphene sheets. Bond lengths between an oxygen atoms and the graphene sheets ranged from 1.48Å to 1.64Å. They are much shorter than the sum of Van der Waals radii of C and O.[24] These results apparently show that OH is chemisorbed on the graphene sheets.

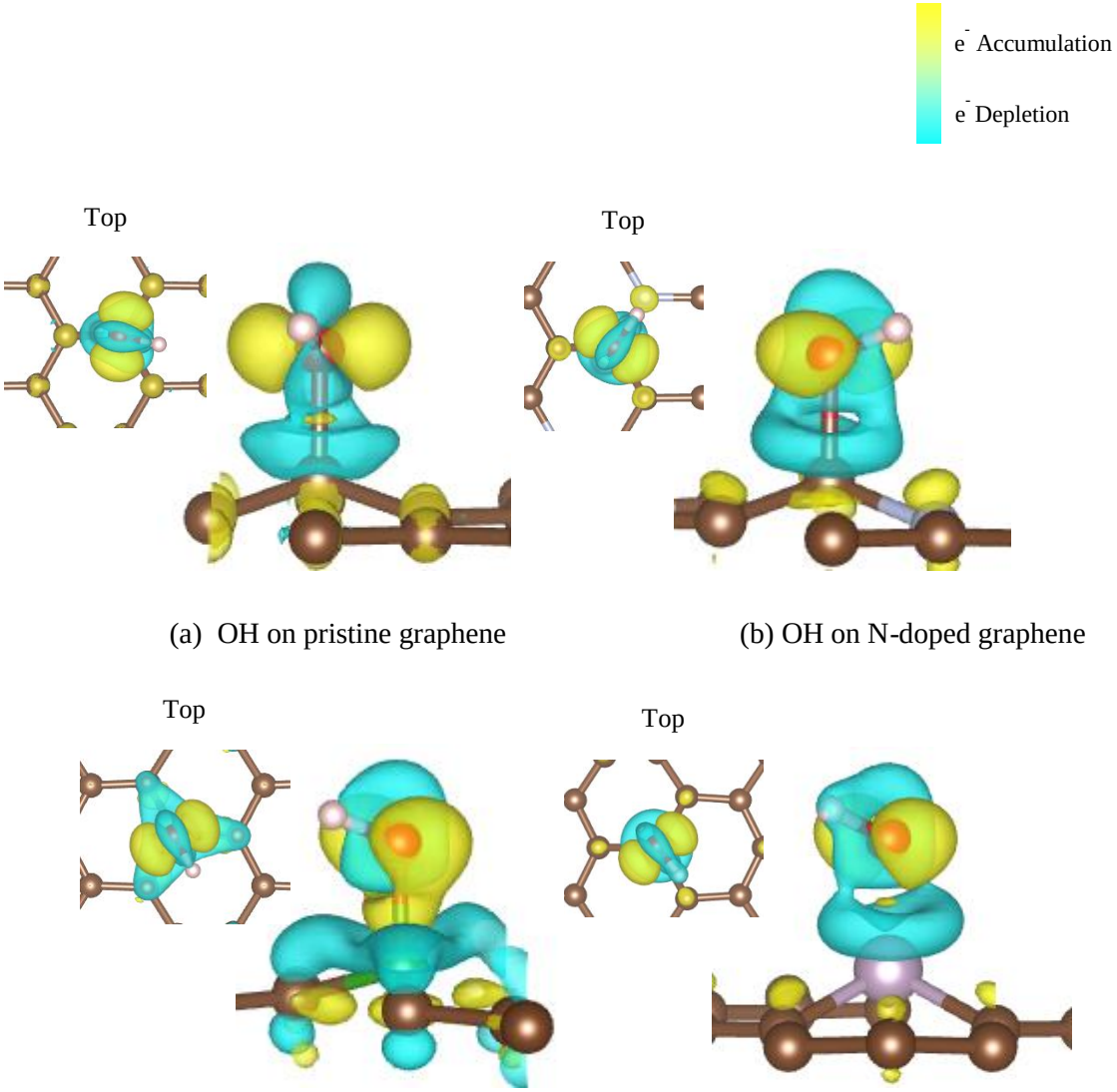

Fig.3.13 Equilibrium geometries and charge density changes for OH adsorbed on (a) pristine graphene, (b) N-doped graphene, (c) B-doped graphene, and (d) P-doped graphene respectively. The yellow (sky-blue) clouds represent an increase (decrease) in charge density, with isosurfaces plotted at $\pm 0.01 e$ Å^{-3}. Brown, grey, green, purple, red, and white spheres represent carbon, nitrogen, boron, phosphorus, oxygen, and hydrogen atoms respectively.

3.5 Oxygen Reduction Reaction Mechanisms

Once O_2 is adsorbed on graphene sheets, oxygen reduction reaction can proceed. We set the $(\sqrt{3}\times\sqrt{3})$ supercell, which has the same three-fold symmetry with the (3×3) supercell, as a model for ORR. Two H_2O molecules are adsorbed on this model system with hexagonal water bi-layer structures as shown in Fig.3.8. We considered four kinds of graphene sheets which are pristine, N-doped, B-doped, and P-doped graphene. One carbon atom is replaced by one nitrogen, boron, and phosphorus atom respectively for doped graphene.

ORR process $(2H_2 + O_2 \rightarrow 2H_2O)$ was simulated in its reverse direction. By keeping removing a hydrogen atom out of the model system at each step, the electron transfer reactions were simulated. At each step, possible intermediates in the ORR process were relaxed to obtain the stable structures, and their energies were calculated. Starting from H_2O*, a hydrogen atom was detached one by one at each intermediate. There can be several intermediates relevant for ORR, which are [OH-H_2O]*, [OH-OH]*, [O-H_2O]*, [OOH]*, and O_2*, where * denotes an adsorption site of O_2 on the graphene surface. With these intermediates, ORR can proceed as follows:

Reaction Path 1

$$O_2 + * \rightarrow O_2^* \tag{3.5}$$

$$O_2^* + H^+ + e^- \rightarrow OOH^* \tag{3.6}$$

$$OOH^* + H^+ + e^- \rightarrow [O + H_2O]^* \tag{3.7 (a)}$$

$$OOH^* + H^+ + e^- \rightarrow HOOH^* \tag{3.7 (b)}$$

$$[O + H_2O]^* + H^+ + e^- \rightarrow [OH + H_2O]^* \tag{3.8 (a)}$$

$$HOOH^* + H^+ + e^- \rightarrow [OH + H_2O]^* \tag{3.8 (b)}$$

$$[OH + H_2O]^* + H^+ + e^- \rightarrow 2H_2O^* \tag{3.9}$$

or

Reaction Path 2

$$O_2 + * \rightarrow 2O^*$$

(3.10)

$$2O^* + H^+ + e^- \rightarrow [O + OH]^* \quad (3.11)$$

$$[O + OH]^* + H^+ + e^- \rightarrow [O + H_2O]^* \quad (3.12\ (a))$$

$$[O + OH]^* + H^+ + e^- \rightarrow 2OH^* \quad (3.12\ (b))$$

$$[O + H_2O]^* + H^+ + e^- \rightarrow [OH + H_2O]^* \quad (3.13\ (a))$$

$$2OH^* + H^+ + e^- \rightarrow [OH + H_2O]^* \quad (3.13\ (b))$$

$$[OH + H_2O]^* + H^+ + e^- \rightarrow 2H_2O^* \quad (3.14)$$

The reaction path 1 starts with an associated oxygen molecule, and the path 2 with dissociated oxygen atoms. As the reactions proceed, it is considered that $(H^+ + e^-)$ is added to the products of the previous reactions. In the case of two possible products from one reactant, both were considered, e.g., Eq.(3.6) → Eq.(3.7(a)) or Eq.(3.7(b)).

To calculate the free energies of the intermediates of ORR, we followed the methodologies in the previous works[53,58]. By setting the reference potential to be that of the SHE, we simply replaced the chemical potential of $(H^+ + e^-)$ with that of $\frac{1}{2}\,H_2$ in gas phase because the free energy change of the reaction $(\frac{1}{2}H_2 \leftrightarrow H^+ + e^-)$ is zero at *pH*=0 in an electrolyte, and 1bar of H_2 in the gas phase at 298K at an electrode potential of *U*=0.

We calculated free energies of the intermediates at *U*=0 and *pH*=0 using $\Delta G = \Delta E + \Delta ZPE - T\Delta S$, where ΔE is the change in internal energy of each reaction from Eqs.3.5 to 3.14, ΔZPE is the difference in zero point energy, T is the temperature, and ΔS is the change in entropy. ΔZPE and ΔS were taken from DFT calculations[59] or standard tables[60,61]. Bias

effect was included in all states involving electrons in the electrode by shifting the energy state as $\Delta G_U = -neU$ where U is the electrode potential and n is the number of electrons involved. More details about the methodologies to construct free energy diagrams can be found in Refs.(53) and (58)[53,58]

Fig.3.14 shows the relaxed structures of ORR intermediates and possible ORR mechanisms on different graphene-based materials. We considered possible reaction paths. Color-filled arrows indicate preferred reaction paths, and unfilled arrows show possible but thermodynamically unfavorable reactions. In the case of pristine graphene, ORR was expected to proceed via a two-electron reaction with the formation of peroxide, while N-doped graphene showed a four-electron reaction rather than the formation of peroxide. These results are consistent with the experimental results[18].

B-doped graphene showed similar intermediates of ORR with N-doped graphene, however, P-doped graphene dissociated an oxygen molecule at the oxygen adsorption step, which was expected from Table 3.2.

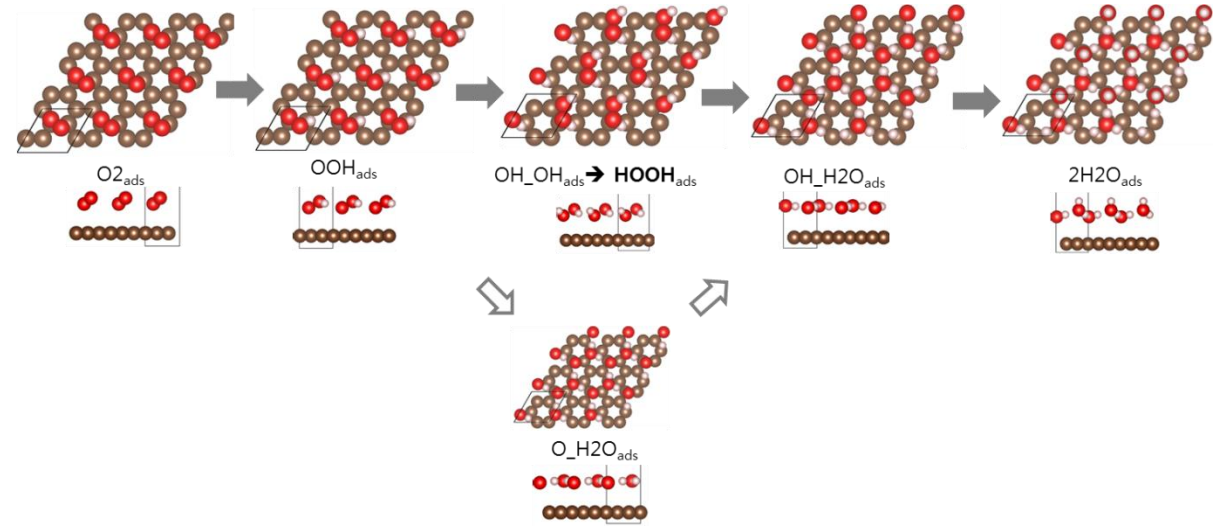

(a) Pristine graphene

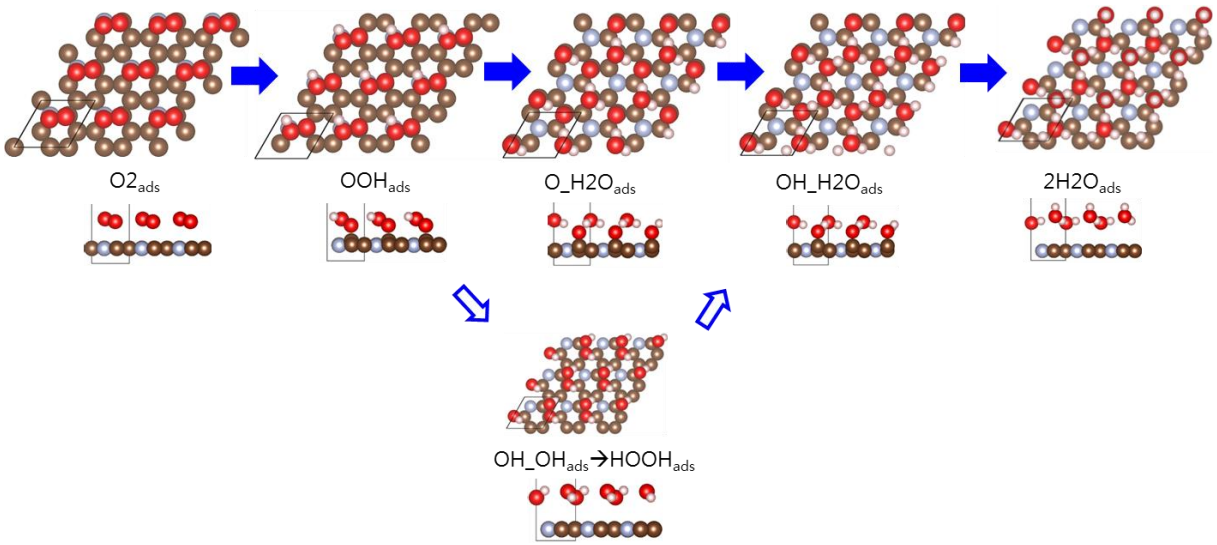

(b) N-doped graphene

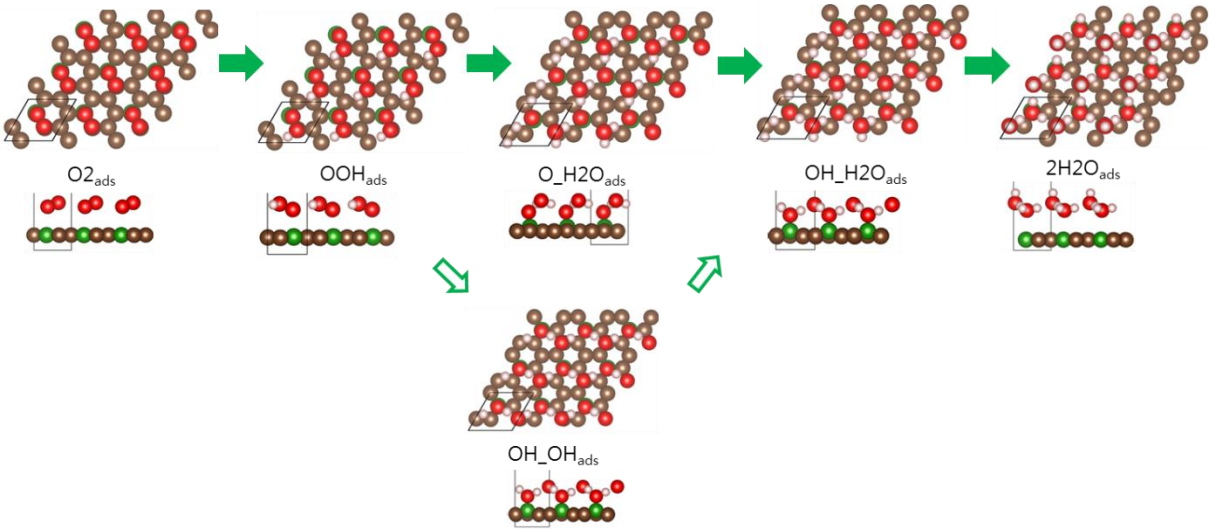

(c) B-doped graphene

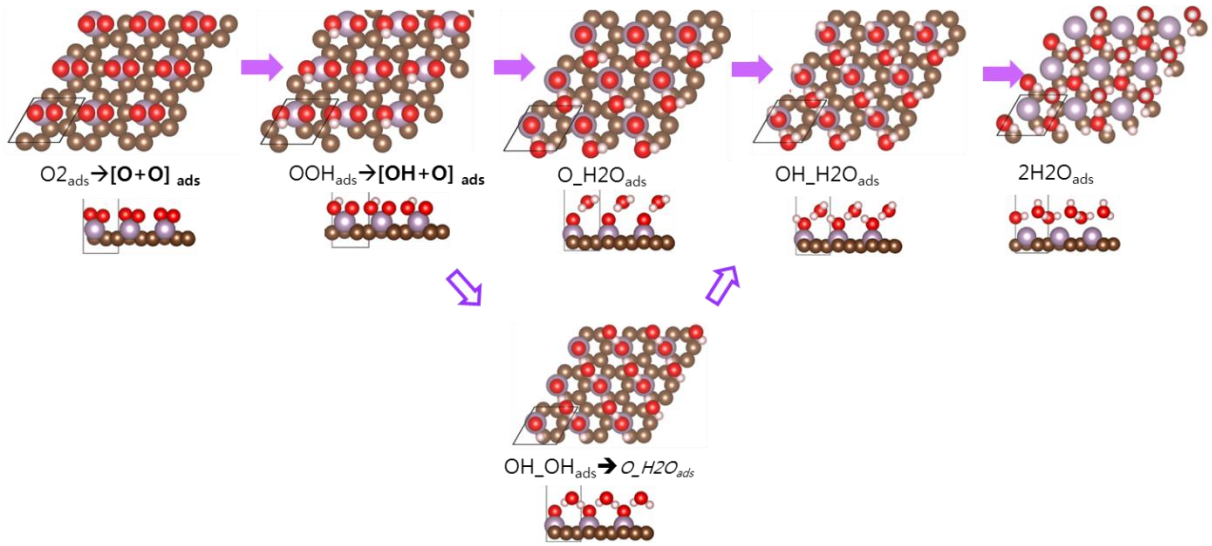

(d) P-doped graphene

Fig.3.14 Proposed oxygen reduction reaction mechanisms on (a) pristine graphene, (b) N-doped graphene, (c) B-doped graphene, and (d) P-doped graphene respectively. Brown, grey, green, purple, red, and white spheres represent carbon, nitrogen, boron, phosphorus, oxygen, and hydrogen atoms respectively.

To compare reaction energies of pristine graphene and N-doped graphene, we present their free energy diagrams for ORR in Fig.3.15. In the case of pristine graphene, G1 is for the successive reactions of

$$\begin{aligned} O_2 + * + 4H^+ + 4e^- &\rightarrow O_2^* + 4H^+ + 4e^- \\ &\rightarrow OOH^* + 3H^+ + 3e^- \\ &\rightarrow HOOH^* + 2H^+ + 2e^- \\ &\rightarrow [OH + H_2O]^* + H^+ + e^- \\ &\rightarrow 2H_2O^* \end{aligned}$$

while G2 is for

$$\begin{aligned} O_2 + * + 4H^+ + 4e^- &\rightarrow O_2^* + 4H^+ + 4e^- \\ &\rightarrow OOH^* + 3H^+ + 3e^- \\ &\rightarrow [O + H_2O]^* + 2H^+ + 2e^- \\ &\rightarrow [OH + H_2O]^* + H^+ + e^- \\ &\rightarrow 2H_2O^* \end{aligned}$$

in Reaction Path 1. The difference between G1 and G2 is only the state $HOOH^*$ versus $[O + H_2O]^*$. As shown in Fig.3.15, HOOH formation is a more favorable reaction on pristine graphene because it is energetically more stable by 1.37 eV. Though the electrode potential *U* is 0 V where overpotential is 1.23 V, reaction $O_2^* + H^+ + e^- \rightarrow OOH^*$ remains uphill. This implies oxygen adsorption and formation of OOH are not spontaneous on pristine graphene. This is consistent with the previous studies, which demonstrated the first electron transfer to the adsorbed oxygen molecule to form superoxide is usually considered as a rate determining step in carbon-based materials.[23,62]

In the case of N-doped graphene, NG1 is for the successive reactions same with G2, while NG2 is

same with G1. Contrary to pristine graphene, HOOH formation is not preferred on N-doped graphene, and all reactions proceed downhill. The remarkable differences between pristine and N-doped graphene are O_2 adsorption and first electron transfer to adsorbed O_2, which are closely related to the O_2 adsorption energies as shown in Table 3.2. By N-doping, the difference of electronegativity between carbon and nitrogen causes partial charges of δ^+ on carbon and δ^- on nitrogen. Carbon atoms with δ^+ can act as adsorption sites for O_2, and facilitate ORR by reducing the overpotential needed in O_2 adsorption. This electronegativity- difference-induced charge redistribution is considered as one of the main reasons for enhanced ORR activity of N-doped graphene.

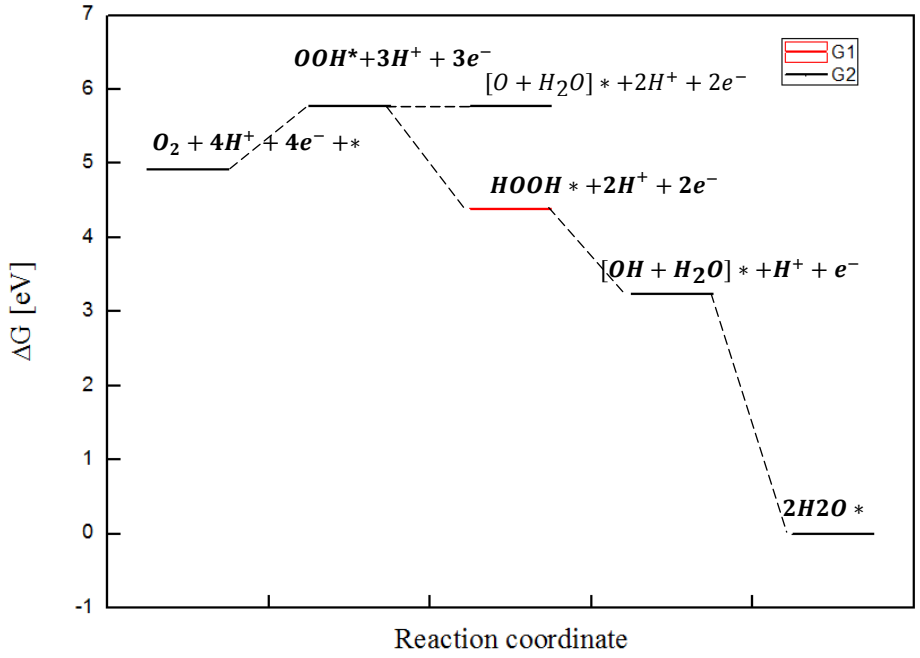

(a) Pristine graphene

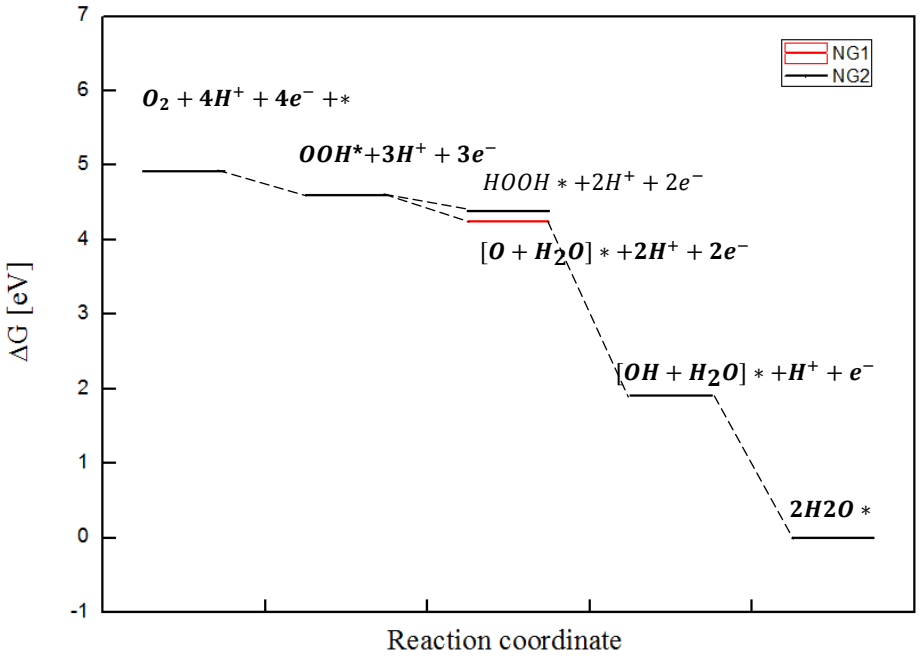

(b) N-doped graphene

Fig.3.15 Free energy diagrams of intermediates in ORR on (a) pristine graphene and (b) N-doped graphene at zero cell potential (U=0 V).

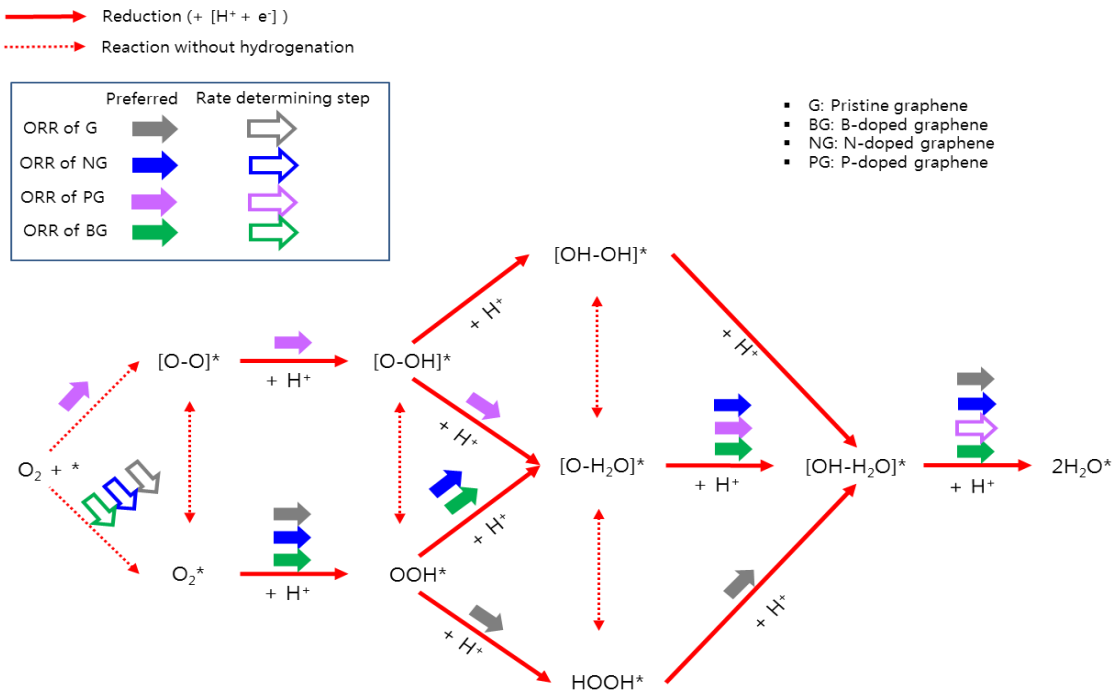

Fig.3.16 Proposed Oxygen reduction reaction mechanisms in $(\sqrt{3}\times\sqrt{3})$ cells of pristine, N-doped, B-doped, and P-doped graphene respectively. Solid and dotted red arrows represent oxygen reduction and reaction without hydrogenation respectively.

In Fig.3.16, we present the alternative ORR intermediates that were calculated in this study. This figure combines results in Fig.3.14 and shows the preferred ORR paths of each graphene-based material. According to the dopant atom, graphene sheets showed different ORR mechanisms. Each suggested reaction mechanism does not mean the sole path but thermodynamically favorable one.

HOOH formation was preferred on pristine graphene, but not on N, B, P-doped graphene during ORR. This result means that doping can alter the reaction mechanisms and enhance the catalytic activity of graphene by inhibiting undesired HOOH formation[63]. This improved ORR catalytic effect can be attributed to doping-induced charge redistribution[64], localized electronic states near Fermi level[47], and reduced band gap[65]. Through this thesis work, we clearly demonstrate that dopants can affect the electronic structures and form positively charged sites favorable for O_2 adsorption which have a relatively lower electronegativity between carbon and dopants (N, B and P).

Chapter 4

Conclusions

This thesis was aimed at understanding of catalytic activity of graphene-based materials in an atomic scale. We demonstrated the quantitative chemical and electrochemical reaction energies of systems obtained by the ab-initio DFT calculations as well as information about stabilized configurations and structures.

In this study, first of all, structures of N-doped graphene were investigated as a function of the nitrogen concentration, and energetically stable structures on the energy convex hull were obtained. With one of these structures as a model, the charge density change by doping was calculated. Besides nitrogen, boron and phosphorus doping were also considered for comparison. We found that the difference in electronegativity between carbon and dopants caused the charge redistributions in graphene sheets and created the charged sites; C: δ^+ and N: δ^- for N-doping, C: δ^- and B: δ^+ for B-doping, and C: δ^- and P: δ^+ for P-doping, respectively. Charged sites with δ^+ in doped graphene acted as adsorption sites for O_2 with stronger adsorption energies than that of pristine graphene. The phosphorus atom incorporated into graphene dissociated the oxygen molecule. This means the doped phosphorus atom weakened the O-O bond.

Furthermore, as O_2 adsorption energy increases, OH adsorption energy also becomes stronger when heteroatom is doped in graphene sheets. Optimized O_2 and OH adsorption energy are necessary for efficient ORR activity because O_2 should be adsorbed well and OH should be removed fast on catalyst sites.

To obtain further insight into ORR mechanisms of graphene-based materials, we calculated the energies of possible ORR intermediates using methodologies in previous works[53,58] As different atoms were incorporated in the graphene, ORR proceeded in different ways. A two-electron reduction

involving HOOH formation was not preferred on N, B, and P-doped graphene but on the pristine graphene. This means that doping of hetero atoms into graphene can alter ORR mechanisms and lead to enhanced catalytic activity for ORR due to the electronic structure modification. Dopants with higher and with lower electronegativity than carbon both can form positively charged sites favorable for O_2 adsorption. We confirm that the atom which has relatively lower electronegativity between carbon and dopants (N, B and P) becomes an O_2 adsorption site. This suggests possibility of a wide range of heteroatom-doped graphene as new efficient catalyst materials.

The main conclusion of this thesis is that we have explored the effect of heteroatom doping on catalytic activity of graphene by using the first principles DFT method. Although the basic analysis of structural properties and catalytic activities of single-atom-doped graphene could yield meaningful insights into catalytic processes, it would perhaps be more interesting to study co-doping effects on catalytic activity. For this, computational methods must play a key role to understand the electrocatalytic reactions of more complex systems in the atomistic scale and develop alternative metal-free catalysts.

References

1 Lewis, N. S. & Nocera, D. G. Powering the planet: Chemical challenges in solar energy utilization. *Proceedings of the National Academy of Sciences* **103**, 15729-15735, (2006).

2 http://www.postech.ac.kr/ce/ecocat/contents_maintheme.htm

3 Neergat, M., Shukla, A. K. & Gandhi, K. S. Platinum-based Alloys as oxygen–reduction Catalysts for Solid–Polymer–Electrolyte Direct Methanol Fuel Cells. *Journal of Applied Electrochemistry* **31**, 373-378, (2001).

4 Greeley, J., Stephens, I. E. L., Bondarenko, A. S., Johansson, T. P., Hansen, H. A., Jaramillo, T. F., Rossmeisl, J., Chorkendorff, I. & Nørskov, J. K. Alloys of platinum and early transition metals as oxygen reduction electrocatalysts. *Nat Chem* **1**, 552-556, (2009).

5 Ji, X., Lee, K. T., Holden, R., Zhang, L., Zhang, J., Botton, G. A., Couillard, M. & Nazar, L. F. Nanocrystalline intermetallics on mesoporous carbon for direct formic acid fuel cell anodes. *Nat Chem* **2**, 286-293, (2010).

6 Bing, Y., Liu, H., Zhang, L., Ghosh, D. & Zhang, J. Nanostructured Pt-alloy electrocatalysts for PEM fuel cell oxygen reduction reaction. *Chemical Society Reviews* **39**, 2184-2202, (2010).

7 Adzic, R. R., Zhang, J., Sasaki, K., Vukmirovic, M. B., Shao, M., Wang, J., Nilekar, A. U., Mavrikakis, M., Valerio, J. & Uribe, F. Platinum monolayer fuel cell electrocatalysts. *Top Catal* **46**, 249-262, (2007).

8 Mani, P., Srivastava, R. & Strasser, P. Dealloyed binary PtM_3 (M=Cu, Co, Ni) and ternary $PtNi_3M$ (M=Cu, Co, Fe, Cr) electrocatalysts for the oxygen reduction reaction: Performance in polymer electrolyte membrane fuel cells. *Journal of Power Sources* **196**, 666-673, (2011).

9 Stamenkovic, V., Mun, B. S., Mayrhofer, K. J. J., Ross, P. N., Markovic, N. M., Rossmeisl, J., Greeley, J. & Nørskov, J. K. Changing the activity of electrocatalysts for oxygen reduction by tuning the surface electronic structure. *Angewandte Chemie* **118**, 2963-2967, (2006).

10 Tang, L., Han, B., Persson, K., Friesen, C., He, T., Sieradzki, K. & Ceder, G. Electrochemical stability of nanometer-scale Pt particles in acidic environments. *Journal of the American Chemical Society* **132**, 596-600, (2009).

11 Shao-Horn, Y., Sheng, W. C., Chen, S., Ferreira, P. J., Holby, E. F. & Morgan, D. Instability of Supported Platinum Nanoparticles in Low-Temperature Fuel Cells. *Top Catal* **46**, 285-305, (2007).

12 Shao, Y., Yin, G. & Gao, Y. Understanding and approaches for the durability issues of Pt-based catalysts for PEM fuel cell. *Journal of Power Sources* **171**, 558-566, (2007).

13 http://austinpowereng.com/Fuel%20cell/PEMFC%20DOE%20AMR%202010.pdf

14 Wang, H., Maiyalagan, T. & Wang, X. Review on Recent Progress in Nitrogen-Doped Graphene: Synthesis, Characterization, and Its Potential Applications. *ACS Catalysis* **2**, 781-794, (2012).

15 Stoller, M. D., Park, S., Zhu, Y., An, J. & Ruoff, R. S. Graphene-Based Ultracapacitors. *Nano Letters* **8**, 3498-3502, (2008).

16 Balandin, A. A., Ghosh, S., Bao, W., Calizo, I., Teweldebrhan, D., Miao, F. & Lau, C. N. Superior thermal conductivity of single-layer graphene. *Nano Letters* **8**, 902-907, (2008).

17 Lee, C., Wei, X., Kysar, J. W. & Hone, J. Measurement of the elastic properties and intrinsic strength of monolayer graphene. *Science* **321**, 385-388, (2008).

18 Qu, L., Liu, Y., Baek, J.-B. & Dai, L. Nitrogen-Doped Graphene as Efficient Metal-Free Electrocatalyst for Oxygen Reduction in Fuel Cells. *ACS Nano* **4**, 1321-1326, (2010).

19 Deng, D., Pan, X., Yu, L., Cui, Y., Jiang, Y., Qi, J., Li, W.-X., Fu, Q., Ma, X., Xue, Q., Sun, G. & Bao, X. Toward N-Doped Graphene via Solvothermal Synthesis. *Chemistry of Materials* **23**, 1188-1193, (2011).

20 Gong, K., Du, F., Xia, Z., Durstock, M. & Dai, L. Nitrogen-Doped Carbon Nanotube Arrays with High Electrocatalytic Activity for Oxygen Reduction. *Science* **323**, 760-764, (2009).

21 Ikeda, T., Boero, M., Huang, S.-F., Terakura, K., Oshima, M. & Ozaki, J.-i. Carbon Alloy Catalysts: Active Sites for Oxygen Reduction Reaction. *The Journal of Physical Chemistry C* **112**, 14706-14709, (2008).

22 Kurak, K. A. & Anderson, A. B. Nitrogen-Treated Graphite and Oxygen Electroreduction on Pyridinic Edge Sites. *The Journal of Physical Chemistry C* **113**, 6730-6734, (2009).

23 Maldonado, S. & Stevenson, K. J. Influence of Nitrogen Doping on Oxygen Reduction Electrocatalysis at Carbon Nanofiber Electrodes. *The Journal of Physical Chemistry B* **109**, 4707-4716, (2005).

24 Okamoto, Y. First-principles molecular dynamics simulation of O2 reduction on nitrogen-doped carbon. *Applied Surface Science* **256**, 335-341, (2009).

25 Sidik, R. A., Anderson, A. B., Subramanian, N. P., Kumaraguru, S. P. & Popov, B. N. O2 Reduction on Graphite and Nitrogen-Doped Graphite: Experiment and Theory. *The Journal of Physical Chemistry B* **110**, 1787-1793, (2006).

26 Vayner, E. & Anderson, A. B. Theoretical Predictions Concerning Oxygen Reduction on Nitrided Graphite Edges and a Cobalt Center Bonded to Them. *The Journal of Physical Chemistry C* **111**, 9330-9336, (2007).

27 Yu, L., Pan, X., Cao, X., Hu, P. & Bao, X. Oxygen reduction reaction mechanism on nitrogen-doped graphene: A density functional theory study. *Journal of Catalysis* **282**, 183-190, (2011).

28 Henkelman, G. & Jonsson, H. A dimer method for finding saddle points on high dimensional potential surfaces using only first derivatives. *The Journal of Chemical Physics* **111**, 7010-7022, (1999).

29 Henkelman, G., Uberuaga, B. P. & Jonsson, H. A climbing image nudged elastic band method for finding saddle points and minimum energy paths. *The Journal of Chemical Physics* **113**, 9901-9904, (2000).

30 Bader, R. F. W. *Atoms in Molecules: A Quantum Theory*. (Oxford University Press, USA, 1994).

31 Zhang, L. & Xia, Z. Mechanisms of Oxygen Reduction Reaction on Nitrogen-Doped Graphene for Fuel Cells. *The Journal of Physical Chemistry C* **115**, 11170-11176, (2011).

32 Lee, K. R., Lee, K. U., Lee, J. W., Ahn, B. T. & Woo, S. I. Electrochemical oxygen reduction on

nitrogen doped graphene sheets in acid media. *Electrochemistry Communications* **12**, 1052-1055, (2010).

33 Han, B., Noh, S. H., Seo, J. K., Kwon, I. H. & Seo, M. H. First Principles Computational Design of High Functional Energy Materials *Korean Industrial Chemistry News* **15**, 39-48, (2012).

34 Sholl, D. & Steckel, J. A. *Density Functional Theory: A Practical Introduction*. (John Wiley & Sons, 2011).

35 Hohenberg, P. & Kohn, W. Inhomogeneous electron gas. *Physical Review* **136**, B864, (1964).

36 Sham, L. & Kohn, W. One-particle properties of an inhomogeneous interacting electron gas. *Physical Review* **145**, 561, (1966).

37 Kresse, G. & Furthmuller, J. *Comput. Mater. Sci.* **6**, 15, (1996).

38 Perdew, J. P., Burke, K. & Ernzerhof, M. *Phys. Rev. Lett.* **77**, 3865, (1996).

39 Kresse, G. & Joubert, D. From ultrasoft pseudopotentials to the projector augmented-wave method. *Physical Review B* **59**, 1758, (1999).

40 Blöchl, P. E. *Phys. Rev. B* **50**, 17953, (1994).

41 Tang, W., Sanville, E. & Henkelman, G. A grid-based Bader analysis algorithm without lattice bias. *Journal of Physics: Condensed Matter* **21**, 084204, (2009).

42 Han, B., Viswanathan, V. & Pitsch, H. First-Principles Based Analysis of the Electrocatalytic Activity of the Unreconstructed Pt(100) Surface for Oxygen Reduction Reaction. *The Journal of Physical Chemistry C* **116**, 6174-6183, (2012).

43 Wu, P., Qian, Y., Du, P., Zhang, H. & Cai, C. Facile synthesis of nitrogen-doped graphene for measuring the releasing process of hydrogen peroxide from living cells. *Journal of Materials Chemistry* **22**, 6402-6412, (2012).

44 Li, Y., Zhao, Y., Cheng, H., Hu, Y., Shi, G., Dai, L. & Qu, L. Nitrogen-Doped Graphene Quantum Dots with Oxygen-Rich Functional Groups. *Journal of the American Chemical Society* **134**, 15-18, (2011).

45 Liu, Z. W., Peng, F., Wang, H. J., Yu, H., Zheng, W. X. & Yang, J. Phosphorus-Doped Graphite Layers with High Electrocatalytic Activity for the O2 Reduction in an Alkaline Medium. *Angewandte Chemie* **123**, 3315-3319, (2011).

46 Endo, M., Hayashi, T., Hong, S.-H., Enoki, T. & Dresselhaus, M. S. Scanning tunneling microscope study of boron-doped highly oriented pyrolytic graphite. *Journal of Applied Physics* **90**, 5670-5674, (2001).

47 Cruz-Silva, E., Lopez-Urias, F., Munoz-Sandoval, E., Sumpter, B. G., Terrones, H., Charlier, J. C., Meunier, V. & Terrones, M. Phosphorus and phosphorus–nitrogen doped carbon nanotubes for ultrasensitive and selective molecular detection. *Nanoscale* **3**, 1008-1013, (2011).

48 Cruz-Silva, E., Cullen, D. A., Gu, L., Romo-Herrera, J. M., Muñoz-Sandoval, E., López-Urías, F., Sumpter, B. G., Meunier, V., Charlier, J.-C., Smith, D. J., Terrones, H. & Terrones, M. Heterodoped Nanotubes: Theory, Synthesis, and Characterization of Phosphorus−Nitrogen Doped Multiwalled Carbon Nanotubes. *ACS Nano* **2**, 441-448, (2008).

49 Shan, B. & Cho, K. Oxygen dissociation on nitrogen-doped single wall nanotube: A first-principles

study. *Chemical Physics Letters* **492**, 131-136, (2010).

50 Kim, H., Lee, K., Woo, S. I. & Jung, Y. On the mechanism of enhanced oxygen reduction reaction in nitrogen-doped graphene nanoribbons. *Physical Chemistry Chemical Physics* **13**, 17505-17510, (2011).

51 Ebbing, D. D. & Gammon, S. D. *General Chemistry*. (Houghton Mifflin, 2009).

52 Karlberg, G. S., Rossmeisl, J. & Nørskov, J. K. *Phys. Chem. Chem. Phys.* **9**, 5158, (2007).

53 Rossmeisl, J., Nørskov, J. K., Taylor, C. D., Janik, M. J. & Neurock, M. *J. Phys. Chem. B* **110**, 21833, (2006).

54 Wang, G., Yang, J., Park, J., Gou, X., Wang, B., Liu, H. & Yao, J. Facile synthesis and characterization of graphene nanosheets. *The Journal of Physical Chemistry C* **112**, 8192-8195, (2008).

55 Ogasawara, H., Brena, B., Nordlund, D., Nyberg, M., Pelmenschikov, A., Pettersson, L. G. M. & Nilsson, A. *Phys. Rev. Lett.* **89**, 276102, (2002).

56 Yu, D., Nagelli, E., Du, F. & Dai, L. Metal-free carbon nanomaterials become more active than metal catalysts and last longer. *The Journal of Physical Chemistry Letters* **1**, 2165-2173, (2010).

57 Bligaard, T., Nørskov, J. K., Dahl, S., Matthiesen, J., Christensen, C. H. & Sehested, J. The Brønsted–Evans–Polanyi relation and the volcano curve in heterogeneous catalysis. *Journal of Catalysis* **224**, 206-217, (2004).

58 Nørskov, J. K., Rossmeisl, J., Logadottir, A., Lindqvist, L., Kitchin, J. R., Bligaard, T. & Jonsson, H. *J. Phys. Chem. B* **108**, 17886, (2004).

59 Kandoi, S., Gokhale, A. A., Grabow, L. C., Dumesic, J. A. & Mavrikakis, M. Why Au and Cu Are More Selective Than Pt for Preferential Oxidation of CO at Low Temperature. *Catalysis Letters* **93**, 93-100, (2004).

60 Weast, R. C. *CRC Handbook of Chemistry and Physics*. (Chemical Rubber, 1970).

61 Atkins, P. W. & De Paula, J. *Atkins' Physical Chemistry*. (Oxford University Press, 2002).

62 Taylor, R. & Humffray, A. Electrochemical studies on glassy carbon electrodes: III. Oxygen reduction in solutions of low pH (pH< 10). *Journal of Electroanalytical Chemistry and Interfacial Electrochemistry* **64**, 85-94, (1975).

63 Yu, T. H., Sha, Y., Liu, W. G., Merinov, B. V., Shirvanian, P. & Goddard III, W. A. Mechanism for Degradation of Nafion in PEM Fuel Cells from Quantum Mechanics Calculations. *Journal of the American Chemical Society* **133**, 19857-19863, (2011).

64 Yu, D., Xue, Y. & Dai, L. Vertically Aligned Carbon Nanotube Arrays Co-doped with Phosphorus and Nitrogen as Efficient Metal-Free Electrocatalysts for Oxygen Reduction. *The Journal of Physical Chemistry Letters* **3**, 2863-2870, (2012).

65 Wang, S., Zhang, L., Xia, Z., Roy, A., Chang, D. W., Baek, J.-B. & Dai, L. BCN Graphene as Efficient Metal-Free Electrocatalyst for the Oxygen Reduction Reaction. *Angewandte Chemie International Edition* **51**, 4209-4212, (2012).

국문요약

제 1 원리 전산을 이용한
그래핀 기반 재료의 연료전지 촉매 거동 연구

미래 사회의 가장 뜨거운 화두 중의 하나인 에너지 문제를 해결할 수 있는 신재생 에너지원으로서 유망한 연료전지는 비싼 백금 촉매 가격, 취약한 내구성 및 안정성, 낮은 촉매 활성도 등으로 인해 상용화에 어려움을 겪고 있다. 따라서 비싼 백금계 촉매를 대체할 수 있는 활성도가 높고 내구성이 좋은 비금속 촉매를 개발하기 위한 연구가 활발히 진행되고 있다. 최근 실험 결과에서는 질소를 도핑한 그래핀이 알칼라인 연료전지에서 기존 백금계보다 우월한 촉매 성능을 보인 것이 보고되기도 하였다.

위의 연구 결과에서 동기를 얻어, 본 논문에서는 제 1원리 전산법을 이용하여 그래핀 물질의 연료전지 산소환원반응에 대한 촉매 거동을 원자 단위 수준에서 밝히고자 하였다. 본 논문에 기술된 내용은 제1원리 범밀도함수 전산법으로 얻어진 정량적인 화학적, 전기화학적 반응 에너지뿐 아니라 대상 물질의 안정화된 구조적 분석을 포함한다. 모든 계산은 Vienna Ab-initio Simulation Package (VASP) 코드를 이용하여 수행하였으며, 전자의 교환상관에너지 (exchange correlation energy)는 GGA PBE 근사를 사용하였다.

우선, 계산을 통해 질소 (N)가 첨가된 그래핀의 열역학적으로 안정한 구조를 구하였다. 이를 통해 얻어진 계산 모델에서 질소 도핑에 따른 전자 밀도 변화를 관찰하기 위해 Bader charge 분석을 하였고, 비교를 위해 붕소 (B)와 인 (P)이 도핑된 그래핀에 대해서도 동일한 계산을 하였다. 탄소 원자와 이종 원자간 전기음성도 차이가 그래핀의 전자 재분포를 야기했고, 이때 δ^+ 전하를 띠게 되는 원자 (질소 도핑의 경우: 탄소, 붕소 도핑의 경우: 붕소, 인 도핑의 경우: 인)가 산소 분자의 흡착 위치로 작용하였다. 중요한 것은 도핑 원소의 전기음성도가 탄소보다 큰지 작은지에 상관 없이 탄소 원자와 이종원자 간 전기 음성도 차이로 인해, 산소 흡착에 유리한 δ^+ 전하를 띠게 되는 위치가 생성된다는 것이다. 이는 순수한 그래핀에 비해 산소 분자의 흡착 에너지를 강화시켜 결과적으로 산소환원반응에 있어서 과전압 (overpotential)을 감소시킴으로써 활성도를 향상시키는 결과를 낳았다. 특히, 도핑된 인 원소는 강한 산소 흡착 에너지와 함께 산소와 산소 원자 사이의 결합을 약화시켜 산소 분자를 해리시키는 거동을 보였다.

산소환원반응에 대한 심화된 이해를 얻고자 반응 중간 생성물의 에너지를 계산하였다. 각각 다른 이종 원소가 도핑된 그래핀에서는 서로 다른 반응 경로를 통해 산소환원반응의 중간 생성물들이 얻어졌다. 질소, 붕소, 인이 도핑된 그래핀에서와 달리 순수한 그래핀에서는 2-전자 환원 반응이 열역학적으로 더 우세할 것으로 예측되었다.

본 연구를 통해 다양한 이종 원소 도핑에 대한 더 넓은 확장과 응용 연구 가능성을 제시할 수 있을 것으로 생각된다. 뿐만 아니라, 향후 두 가지 이상 원소가 도핑된 보다 복잡한 그래핀 구조의 촉매 기구에 대해 도핑 원소들 간의 시너지 효과를 연구한다면, 더욱 흥미롭고 유익한 결과를 얻을 수 있을 것으로 기대된다.

핵심어: 연료전지, 제1원리 전산, 범밀도 함수 이론, 산소환원반응, 그래핀

감사의 글 (Acknowledgement)

먼저 2 년간의 석사 학위 과정 동안 양자전산이라는 새로운 학문 분야로 이끌어 주시고 공부할 수 있게 지도해 주신 한병찬 교수님께 깊은 감사의 말씀을 드립니다. 그리고 한없이 부족한 논문이지만 완성되기까지 새로운 아이디어와 유익한 조언을 주신 김호영 박사님, 김하석 교수님께도 감사의 인사를 드립니다.

2 년이라는 시간 동안 눈물과 웃음을 함께 나눈 우리 AICODES 멤버들에게는 우정과 감사의 인사를 함께 담아 전합니다. 정말 믿음직스럽고 책임감 있게 연구실의 큰 일들을 도맡아 해준 준교 오빠, AICODES 에 없어서는 안 되는 능력자이자 분위기 메이커 승효, 두 말이 필요 없는 우리의 학문적, 정신적 멘토 서민호 박사님, 어려운 분야의 프로젝트를 맡았지만 불만 갖지 않고 열심히 잘 해주고 있는 고마운 후배들 상흠이, 준희, 그리고 그 동안 AICODES 를 스쳐간 혜민언니, 혜림이, Abhishek, 기돈이에게도, 그들의 보이지 않는 도움과 배려가 있었기에 이 논문이 나올 수 있었다는 말을 꼭 전하고 싶습니다.

석사과정에서 전공한 양자전산이라는 학문은 열역학, 재료공학, 물리학, 화학 등 여러 기초 학문에 대한 지식과 이해가 요구되는 포괄적인 학문이었습니다. 석사과정의 짧은 시간 동안 비록 빙산의 일각조차 깨우치지 못했지만, 다양한 학문 배경을 지닌 동료들이 있었기에 무사히 학위 과정을 마칠 수 있었습니다. 원교, 가영이, 순욱 오빠, 하영이, 동휘, 은영이, 영준 오빠, 유미, 일연 오빠, Jakkid, Kriangsak, Prakash 에게도 고맙다는 인사를 전합니다.

휴직 후 다시 시작한 공부였을 뿐 아니라 신생 학교의 1 기 입학생이었기에 불안과 기대를 동시에 안고 대학원 생활을 시작했습니다. 힘든 순간마다 진심 어린 조언과 격려를 해준 포항공대 박사과정 선미와 한양대 박사과정 정현이에게 고마운 마음을 전합니다.

좀더 쓰임이 있는 사람이 되고자 고심 끝에 결심한 진학을 뒤에서 응원해 주신 POSCO 임광수 부장님, 김광영 팀장님, 김종국 공장장님을 비롯한 여러 선배님들과 동기, 후배님들께도 진심으로 감사의 말씀을 드리고 싶습니다.

마지막으로 가장 사랑하는 우리 가족들, 특히 고집 센 큰 딸의 뒤늦게 다시 시작한 공부를 묵묵히 지켜봐 주시고, 힘들었던 순간에 넓은 품과 두 팔로 보듬어 용기를 주셨던 아버지, 어머니께 진심을 다해 사랑과 감사를 전합니다.

아버지, 어머니 고맙습니다. 그리고 사랑합니다.

Curriculum Vitae

Name: In Hye Kwon
Birth Date: 1985.09.30

Education

2004-2008 B.S., Department of Materials Science & Engineering, Hanyang University
2011-2013 M.S., Department of Energy Systems Engineering, DGIST

Work Experience

2008-2011 Cold Rolling Technical Development Team, Department of Cold Rolling, POSCO

Publication

Dong Hwan Kim, In Hye Kwon, Cham Kim, Byungchan Han, Hee-Joong Im, Hoyoung Kim*,
Tellurium-evaporation-annealing for p-type bismuth–antimony–telluride thermoelectric materials,
Journal of Alloys and Compounds 548 (2013) 126-132